metals

MDPI

Article

Analysis of Oxide Layer Formation During Oxidation of AISI 4140 Steel at 1000 °C over Exposure Time

Matheus O. Carvalho [1,*], Lioudmila A. Matlakhova [1], Sérgio N. Monteiro [2], Rosane S. T. Manhães [1] and Natalia A. Palii [3]

[1] Advanced Materials Laboratory, Science and Technology Center, Darcy Ribeiro State University of Northern Fluminense—Rio de Janeiro (UENF), Campos dos Goytacazes 28013-602, RJ, Brazil; lioudmila@uenf.br (L.A.M.); toledo@uenf.br (R.S.T.M.)
[2] Department of Materials Science, Military Institute of Engineering (IME), Rio de Janeiro 22290-270, RJ, Brazil; sergio.neves@ime.eb.br
[3] Laboratory of New Metallurgical Processes and Alloys, A. A. Baikov Institute of Metallurgy and Materials Science, Russian Academy of Sciences, 119334 Moscow, Russia; palii@imet.ac.ru
* Correspondence: matheus.o.carvalho@hotmail.com

Abstract: The high-temperature shaping of steels is accompanied by the formation of surface scales composed of oxide layers. However, the oxidation kinetics and morphology of these scales remain poorly understood. This study analyses the formation of oxide layers on AISI 4140 steel at varying oxidation times (20, 40 and 60 min) at 1000 °C. The analysis revealed the presence of hematite, magnetite, and transformed wustite in the oxide layers, along with clusters of alloying element oxides, predominantly chromium and iron oxide ($FeCr_2O_4$). There was a direct correlation between the duration of the oxidation process and the thickness of the scale and the number of defects observed in the material. The coating layer of alloying element oxides demonstrated insufficient adhesion to the steel substrate. Similarly, the oxides of alloying elements within this layer exhibited low cohesion among themselves. The alloying elements are present in all oxide layers, but in greater quantity in the layer in contact with the steel substrate, where a reduction in their concentrations was observed over time. This indicates that the alloying elements tend to disperse as the thickness of the alloying element oxide layer increases over time.

Keywords: hot oxidation; scale; iron oxides; alloying elements; carbon steel

check for updates

Citation: Carvalho, M.O.; Matlakhova, L.A.; Monteiro, S.N.; Manhães, R.S.T.; Palii, N.A. Analysis of Oxide Layer Formation During Oxidation of AISI 4140 Steel at 1000 °C over Exposure Time. *Metals* **2024**, *14*, 1251. https://doi.org/10.3390/met14111251

Academic Editors: Chao Liu, Zhongyu Cui and Tianliang Zhao

Received: 10 September 2024
Revised: 21 October 2024
Accepted: 24 October 2024
Published: 4 November 2024

Copyright: © 2024 by the authors. Licensee MDPI, Basel, Switzerland. This article is an open access article distributed under the terms and conditions of the Creative Commons Attribution (CC BY) license (https://creativecommons.org/licenses/by/4.0/).

1. Introduction

In steel mills, the manufacturing process for semi-finished carbon steel products employs high-temperature mechanical shaping techniques, such as the hot rolling process. During this process, the carbon steel is heated to approximately 1000 °C to enhance its malleability. This enables the carbon steel to be plastically deformed, thus allowing it to be shaped into the desired geometry [1,2].

The high-temperature process presents a challenge due to the formation of a layer of metal oxides, known as scale. Scale is the term used to describe an unwanted layer of metal oxides that forms on the surface of carbon steel during hot working processes. The scale is mainly composed of oxides of metals present in the steel composition, primarily the following iron oxides: wustite (FeO), magnetite (Fe_3O_4), and hematite (Fe_2O_3) [3,4].

Pure iron heated in oxygen at 1 atm and below 575 °C predominantly forms magnetite. However, it should be noted that hematite also forms. Wustite is only observed at temperatures above 575 °C and is found in a region of transformed wustite at room temperature. It decomposes into magnetite and pure iron. Furthermore, wustite can be found at temperatures below 575 °C. This phase does not require high cooling rates to obtain its metastable form [5].

The phase composition and thickness of the scale formed on the steel surface during hot forming processes is influenced by several factors, including the following [6,7]:

(i) the process temperature;
(ii) the exposure time at high temperatures;
(iii) the oxidizing environment;
(iv) the steel's specific alloy composition; and
(v) the cooling rate.

The chemical composition of steel is of paramount importance in determining the kinetics and morphology of scale formation. Alloying elements and impurities exert a profound influence on both oxidation kinetics and final scale morphology. This has made it a significant challenge to gain a comprehensive understanding of this phenomenon, given that each element exhibits distinct behavior during steel oxidation [8,9].

Steel manufacturers incorporate certain alloying elements, such as chromium, silicon, and aluminum, into the steel's composition to prevent oxidation and diminish the thickness of the scale. The reason for this inclusion is that these elements, which have a greater affinity for oxygen than Fe, form a protective oxide layer on the steel surface. This process is clearly demonstrated by the findings of studies [10–12]. The formation of a protective alloying element oxide layer is dependent on the proportion of these elements incorporated into the steel composition. Alloying elements are unlikely to form a continuous film across the entire scale when present in low quantities. Conversely, they accumulate in specific regions. The wustite layer near the scale/substrate region and within the steel is a case in point. This accumulation contributes to a phenomenon known as internal oxidation. It is important to note that even relatively low concentrations of alloying elements can significantly impact the kinetics of other oxide formation in the scale, even in the absence of a continuous film [13,14].

Nowadays, the most commonly used methods to study the oxidation processes and scale structure of steel are electron microscopy, X-ray diffraction and optical microscopy.

However, it should be noted that in recent years, Raman spectroscopy has been increasingly applied to the study of in situ oxidation processes (oxide formation, coatings) at high temperatures. A number of articles present the results of successful applications of Raman spectroscopy, including in-depth study of the structure of oxides and the scale formation of various alloys, phase transformations in ceramics, spinels, and so on [15–19]. The agreement between Raman and X-ray data has been found in the in situ study of the structural changes of Ce–Pr–O oxides in hydrogen [16] and in the high pressure study of Cr_2O_3 obtained by oxidation at high temperatures [17].

However, this method offers more possibilities than X-ray diffraction. It was stated in [18] that in situ Raman imaging of HT reactions also offers the possibility to systematically investigate the influence of heating and cooling cycles on textural and mineralogical re-equilibration with only one experiment and by analysing the very same sample. The authors of [19] have successfully combined a fibre-optic Raman probe with the concept of high-temperature Raman spectroscopy to perform in situ high-temperature Raman analysis of the structure of glass and slag samples at temperatures up to 1400 °C. In [20], in situ Raman spectroscopy was shown to be a powerful tool for studying cation disorder in spinel-structured minerals. Raman spectroscopy can, therefore, be used to study real-time changes in chemical composition under high-temperature conditions, providing a more precise insight into these processes.

The main objective of this paper is to examine the impact of chemical composition and varying exposure times at 1000 °C on the oxide layers formed on the surface of AISI 4140 carbon steel, analysed at room temperature. This will be achieved by utilizing similar industry heating and cooling processes in atmospheric conditions.

2. Materials and Methods

The research used AISI (Groupo Goncalves Dias S/A, São Paulo, Brazil) 4140 steel sheets as the material, sourced from a commercial supplier. Table 1 presents the chemical

composition of the steel. The specimens were made with a thickness of 17 mm and a dimension of 7 × 7 mm in length and width, respectively. The specimens were subjected to a two-step cleaning process, comprising sanding and polishing, prior to the oxidation tests. This process was necessary to remove surface inconsistencies and discontinuities that could impede the formation and analysis of the oxide layer.

Table 1. Chemical composition of AISI 4140 low alloy carbon steel (wt%) provided by the manufacturer.

C	Mn	Si	P	S	Cr	Ni	Mo	Al	Cu	Fe
0.386	0.851	0.230	0.021	0.024	0.866	0.111	0.169	0.030	0.298	rest.

The steel specimens were subjected to an oxidation treatment in a muffle furnace (EDG Equipament brand, model EDG 3P-S 3000, internal dimensions: W = 150 × H = 100 × D = 200 mm and volume of 3 L, São Paulo, Brazil), following the discontinuous thermogravimetry method. This method consists of studying the oxidation kinetics through discontinuous weighing. The specimens were exposed to atmospheric air, with a heating rate of 20 °C/min until the temperature reached 1000 °C. At the peak temperature, the specimens were held at constant temperature for the following periods: 20, 40, and 60 min. Subsequently, the specimens were cooled to room temperature.

The samples were weighed and tested in crucibles (CasaLab, Belo Horizonte-MG, Brazil) to prevent any loss of material. The test results were then plotted against oxidation kinetics.

Besides the mass gain expressed as mg/cm^2, it was also expressed as a percentage (%) according to the following formula:

$$\%GM = ((GM_{(i+20)} - GM_i)/GM_i) \times 100\% \quad (1)$$

where, i = 0, 20, 40 min.

The thicknesses of the oxide films formed were measured using lmageJ software 1.54i (accessed on 3 March 2024) (National institutes of Health, Bethesda, MD, USA). The 36 measurements taken at different points along the entire 7 mm length of the scales were used to calculate average thickness.

Following the oxidation treatment, the specimens were subjected to examination to study the formed oxide layers. The X-ray diffraction (XRD) (Shimadzu Corporation, Kyoto, Japan) analysis was conducted to identify the different phases present. To this end, an unprecedented analysis was conducted on three areas of the scale for all the conditions analysed. The initial analysis was conducted on the exterior of the scale, the area in direct contact with the oxidizing atmosphere. The second analysis was conducted on the interior of the scale, the area in contact with the metal substrate. The detachment of the scale from the metal substrate during the cooling process made this possible. The final analysis was conducted on the residual scale, which remained attached to the substrate. This area is referred to as the residual layer on the substrate.

To protect the oxide layer and permit the evaluation of cross-section samples, the specimens were consecutively embedded in graphite-based conductive phenolic resin. The specimen's surface was subsequently sanded and polished to facilitate the examination of the microstructure and morphology of cross-sections of the oxide layer, which was examined by scanning electron microscopy (SEM) (Shimadzu Corporation, Kyoto, Japan) and optical microscopy (OM) (Olympus Corporation, Tokyo, Japan). We mapped and analysed the distribution of chemical elements within the oxide layer using energy dispersive spectroscopy (EDS) (JEOL Ltd., Tokyo, Japan), employing both mapping and point analysis techniques.

3. Results and Discussions

3.1. Mass Gain

Table 2 and Figure 1 show the mass gain after the oxidation test for 4140 steel. As the oxidation time increases, the mass gain of the samples increases.

Table 2. Average mass increase in mg/cm^2 at 1000 °C as a function of exposure time to oxidation in atmospheric air for 4140 steel.

	20 min	40 min	60 min
Mass	16.4416	18.9854	20.5617
Standard Deviation	1.0367	1.1546	0.3031

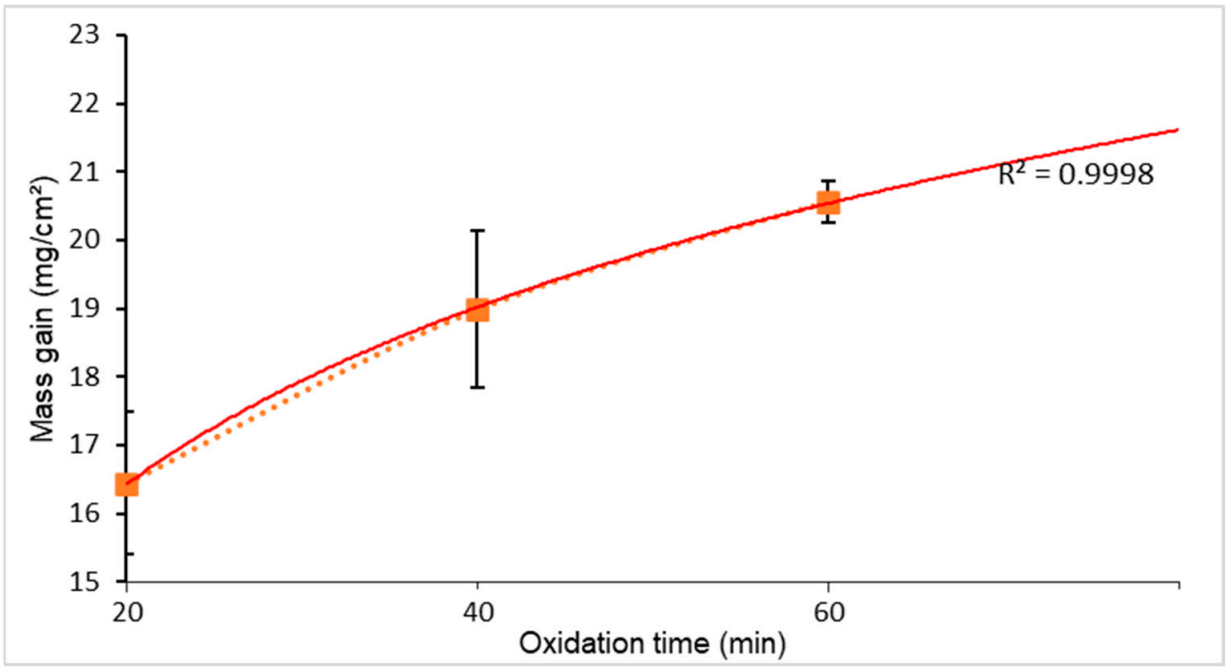


Figure 1. Average mass gain at 1000 °C as a function of exposure time to oxidation, in atmospheric air, of 4140 steel. Actual result, dashed line; parabola trend line with regression (R^2), solid line. The orange square is the point that indicates the analyzed test time, as well as the standard deviation.

With regard to Figure 1, it should be noted that the actual curve is formed by the dotted line. The solid line is the trend line. It can be seen that both are very close to each other. The regression value "R^2" is approximately 1, which makes this regression very accurate.

Table 3 shows the percentage increase in mass gain as a function of oxidation time. It can be observed that in the first 20 min, at isothermal temperature, the percentage increase in the mass gain is low, then increases significantly in the period from 20 to 40 min, and then decreases in the period from 40 to 60 min. Dubiel and Zukrowski (2019) [21], highlight that the reduction in mass gain over time is directly related to the growth of oxide layers that have a tendency to form a barrier, hindering the diffusion of elements and consequently reducing their diffusion rates and increasing the oxidation resistance of the steel. At 1000 °C, as the oxidation time increases, the thickness of the oxide layers also tends to increase, reducing the diffusion rate of the elements and causing the mass gain to stabilize until it becomes practically constant with time. It can be concluded that the oxidation kinetic curve of 4140 steel follows the parabolic law. The oxidation kinetics are more intense after 20 min, at isothermal temperature, where the mass gain is greater, then the kinetics are reduced, thus reducing the mass gain. Similar results were observed in the research of Sadique et al. (2000) [22].

Table 3. Percentage increase in mass gain at 1000 °C as a function of exposure time to atmospheric oxidation of 4140 steel.

0–20 min	20–40 min	40–60 min
1.57	15.47	8.30

Another relevant factor in the variation of the mass gain of 4140 steel is the Cr content of the steel. Considering the results of the work of Genève et al. (2008) [9], the Cr content present in 4140 steel has the tendency to increase its resistance to oxidation by forming a continuous Cr_2O_3 film close to the metal substrate, which hinders the diffusion of iron to the more outer regions of the scale and the diffusion of oxygen to the more inner regions. The reduction in the diffusion rate of these elements tends to reduce the mass gain in the oxidation process.

3.2. Phase Analysis

Figures 2a, 3a and 4a show the XRD pattern from the external surface of the oxide layer of the AISI 4140 steel specimen after 20, 40 and 60 min of oxidation at 1000 °C, respectively.

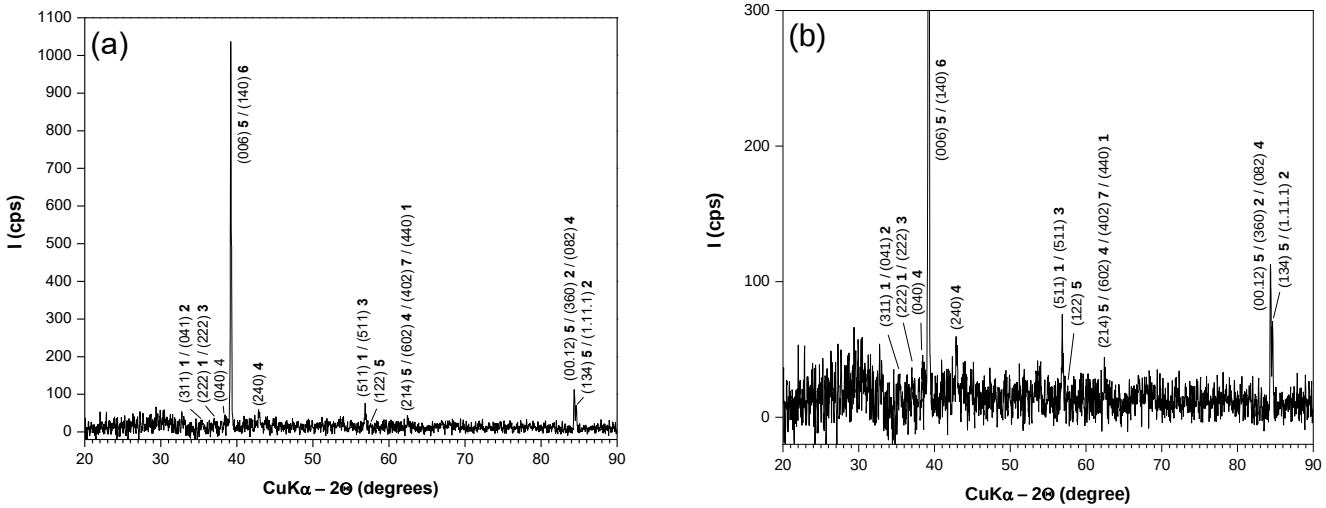


Figure 2. XRD pattern of the external layer of AISI 4140 steel oxidized for 20 min at an isothermal temperature of 1000 °C in atmospheric air, with subsequent air cooling: (**a**) lower magnification; (**b**) higher magnification.

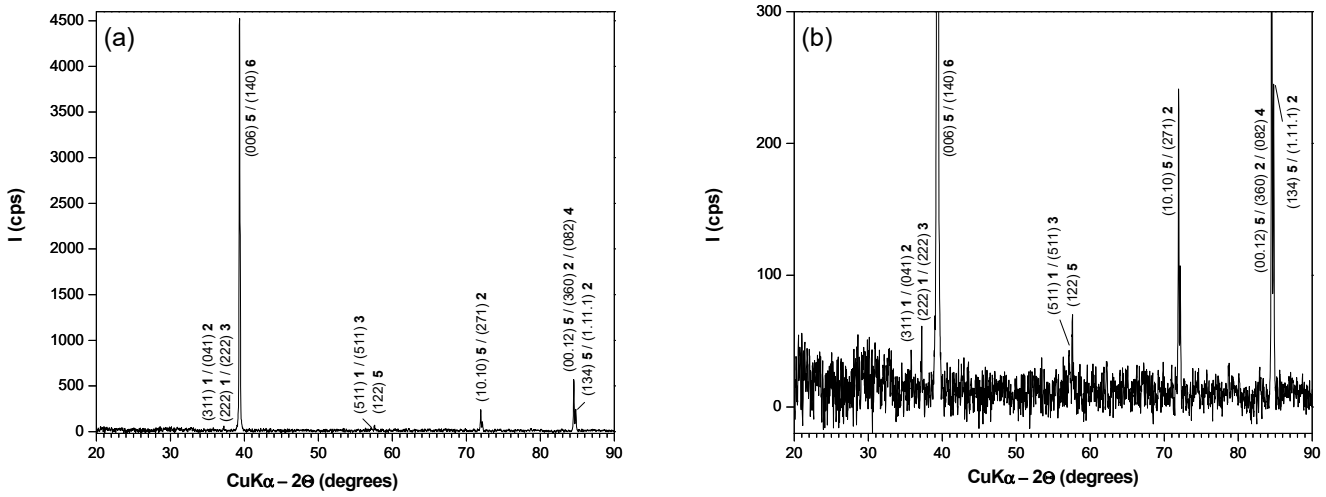


Figure 3. XRD pattern of the external layer of AISI 4140 steel oxidized for 40 min at an isothermal temperature of 1000 °C in atmospheric air, with subsequent air cooling: (**a**) lower magnification; (**b**) higher magnification.

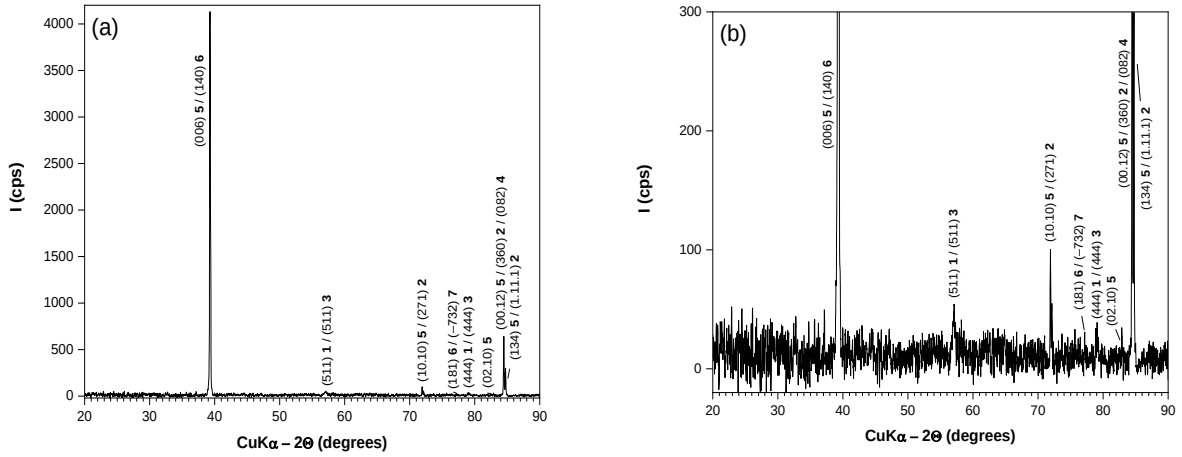


Figure 4. XRD pattern of the external layer of AISI 4140 steel oxidized for 60 min at an isothermal temperature of 1000 °C in atmospheric air, with subsequent air cooling: (**a**) lower magnification; (**b**) higher magnification.

The major phase of AISI 4140 steel is Fe_2O_3, as indicated by its peak intensity. The corresponding peaks of the crystallographic planes (006), (0012) and (134) were identified with the following relative intensities (RIs): 100%, 10.88%, 6.80% at 20 min; 100%, 12.69%, 5.40% at 40 min; and 100%, 15.53% and 7.21% at 60 min, respectively.

The expected high intensity peaks for Fe_2O_3 in powder, such as (104) (IR = 100%) and (110) (IR = 72.1%), were not observed at the corresponding positions (33.16° and 35.63° 2θ using Cu–Kα radiation) according to the reference pattern PDF Card No: 01-087-1166 [23]. Instead, a peak of high intensity corresponding to (006) of the Fe_2O_3 plane (IR = 100%) was observed, together with others of much lower intensity. This indicates a preferential crystallographic orientation of the hematite phase with regard to the underlying substrate surface.

Figures 2b, 3b and 4b show enlarged views (Y-axis intensity) of the XRD pattern obtained from the outer surface of the oxide layer of the AISI 4140 steel sample after 20, 40 and 60 min of oxidation at 1000 °C, respectively.

The XRD analysis definitively revealed the presence of Fe_2O_3, along with Fe_3O_4, manganese oxide (Mn_2O_3), iron silicate ($FeSiO_3$) and possible traces of molybdenum oxide (MoO_3) and chromium–iron oxide compound ($FeCr_2O_4$). These identifications were made by comparing the observed peaks with reference data sheets 01-088-0315, 01-071-0635, 01-082-1834, 01-078-4613 and 01-075-3312, respectively [24–28]. The number of peaks associated with the identified phases remained constant regardless of the oxidation time. This finding proves that the oxidation time had no effect on the preferential orientation of the oxide crystallites with respect to the substrate surface.

The phase identification is numbered according to the following legend:

1. Fe_3O_4
2. MoO_3
3. $FeCr_2O_4$
4. Mn_2O_3
5. Fe_2O_3
6. Fe_2SiO_4
7. $FeSiO_3$
8. $Fe_2Al_2O_4$
9. CuO
10. NiO
11. NiO_2
12. $Mn_{2.97}Fe_{0.03}0_4$
13. Cu_2O

Figures 5–7 show the XRD pattern obtained from the inner surface of the oxide layer formed on the AISI 4140 steel specimen after 20, 40 and 60 min of oxidation at 1000 °C, respectively.

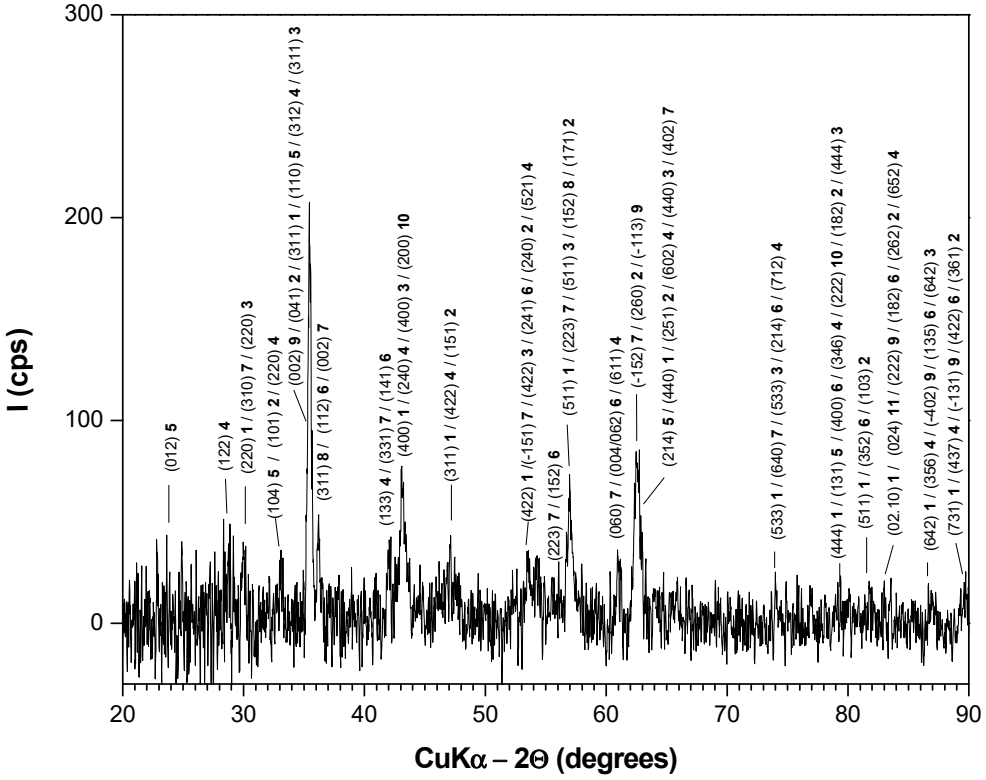


Figure 5. XRD pattern of the internal layer of AISI 4140 steel oxidized for 20 min at an isothermal temperature of 1000 °C in air, followed by air cooling.

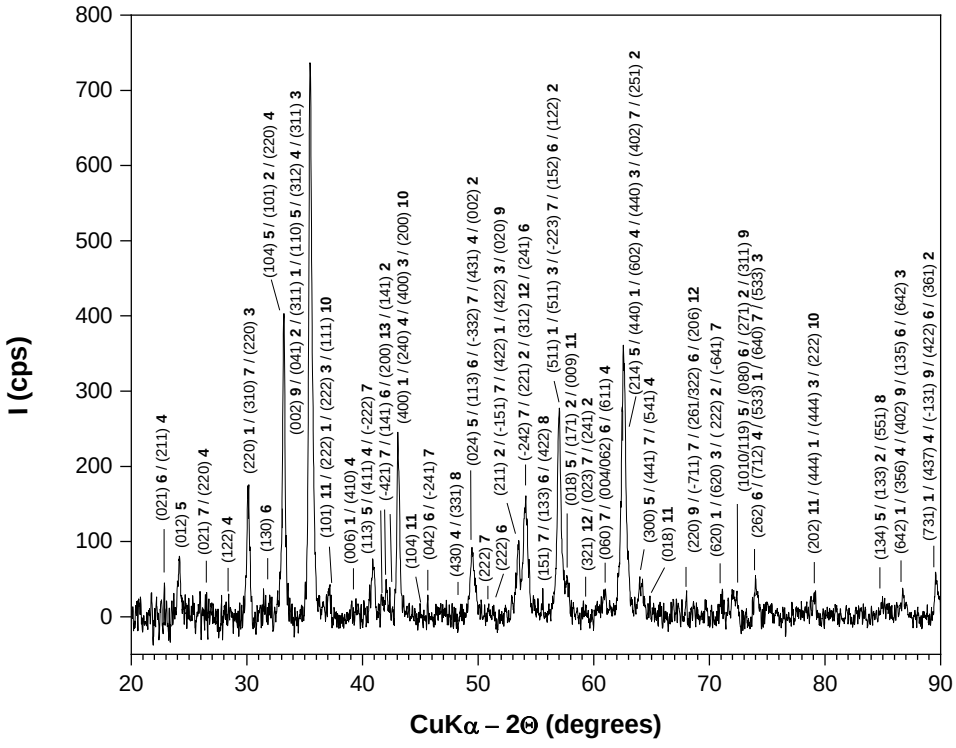


Figure 6. XRD pattern of the internal layer of AISI 4140 steel oxidized for 40 min at an isothermal temperature of 1000 °C in air, followed by air cooling.

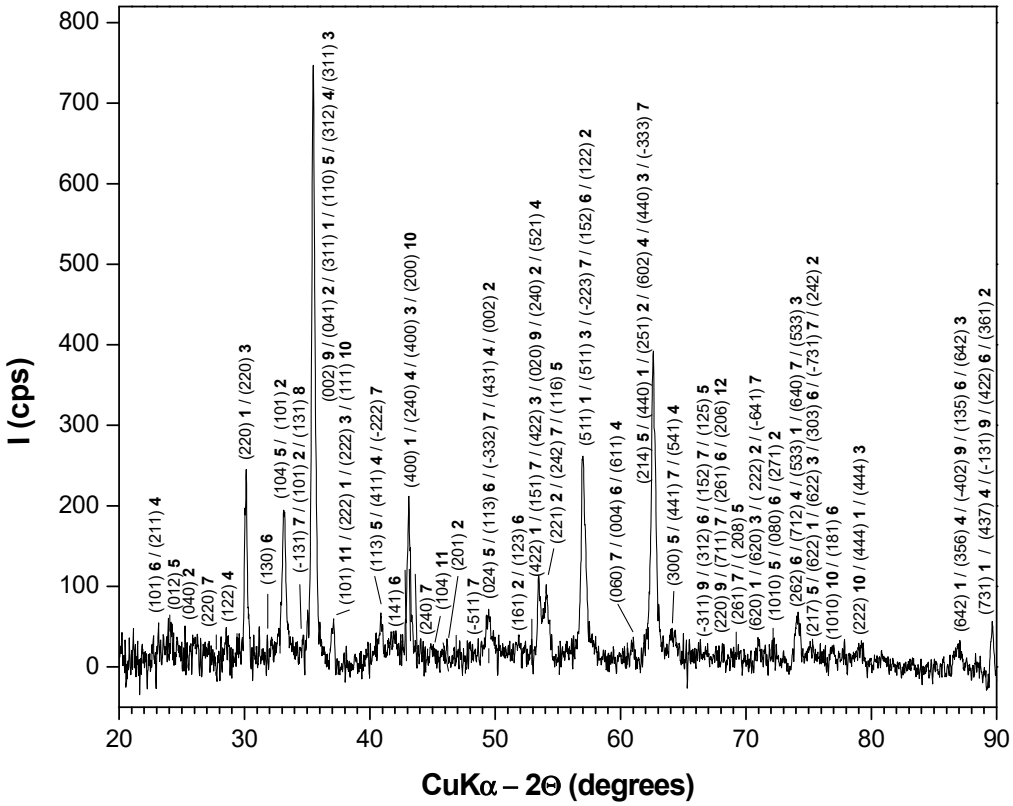


Figure 7. XRD pattern of the internal layer of AISI 4140 steel oxidized for 60 min at an isothermal temperature of 1000 °C in air, followed by air cooling.

The internal oxide layer contains all the oxides of the alloying elements present in the AISI 4140 steel composition. However, the following five phases were identified as the following dominant phases: Fe_3O_4, $FeCr_2O_4$, Fe_2O_3, fayalite (Fe_2SiO_4) (PDF card no.: 01 -070-1861 [29]) and $FeSiO_3$.

The internal oxide layer is primarily composed of Fe_3O_4. This is evident from the high intensity of the peaks associated with its characteristic crystallographic planes, in particular those corresponding to the (311), (400), (511) and (440) planes. Furthermore, Fe_2O_3 was identified by the presence of strong peaks associated with the (214), (104) and (110) planes.

The higher intensity peaks observed in the XRD pattern for the internal oxide layer unquestionably correspond to those expected for powdered Fe_3O_4 according to the reference data sheet (PDF Card No: 01-088-0315). These peaks correspond to the crystallographic planes (311) (IR = 100%) and (400) (IR = 20.7%) observed at positions 35.52° and 43.17° 2θ (Cu–Kα), respectively. These peaks (IR = 100%) observed in the XRD pattern obtained for AISI 4140 steel, match perfectly with the reference sheet data. However, the presence of other phases is also observed and will undoubtedly influence the overall peak intensities based on their relative abundance. This proves that Fe_3O_4 does not have a preferential crystallographic orientation with respect to the substrate surface, while other phases do.

The high intensity peaks of Fe_2O_3 can be attributed to the thin oxide layer of AISI 4140 steel, which allows XRD radiation to penetrate deeper into the scale. The presence of Fe_2SiO_4 and $FeSiO_3$ is confirmed by several low-intensity peaks and/or broad peaks, together with other oxides. Furthermore, $FeCr_2O_4$ is consistently observed in the same plane together with Fe_3O_4.

The inner layer, as seen in Figures 5–7, shows peaks of lower absolute intensity than the outer layer in Figures 2–4. This clearly indicates that a greater number of crystallographic planes are involved in the diffraction pattern. This means that the crystallites within this layer are randomly oriented in space, i.e., they have lost their preferred orientation.

Furthermore, it was evident that the overall peak intensity diminished as the number of peaks increased with prolonged oxidation.

Figures 8–10 show the XRD pattern obtained from the residual oxide layer on the AISI 4140 steel substrate after 20, 40 and 60 min oxidation at 1000 °C.

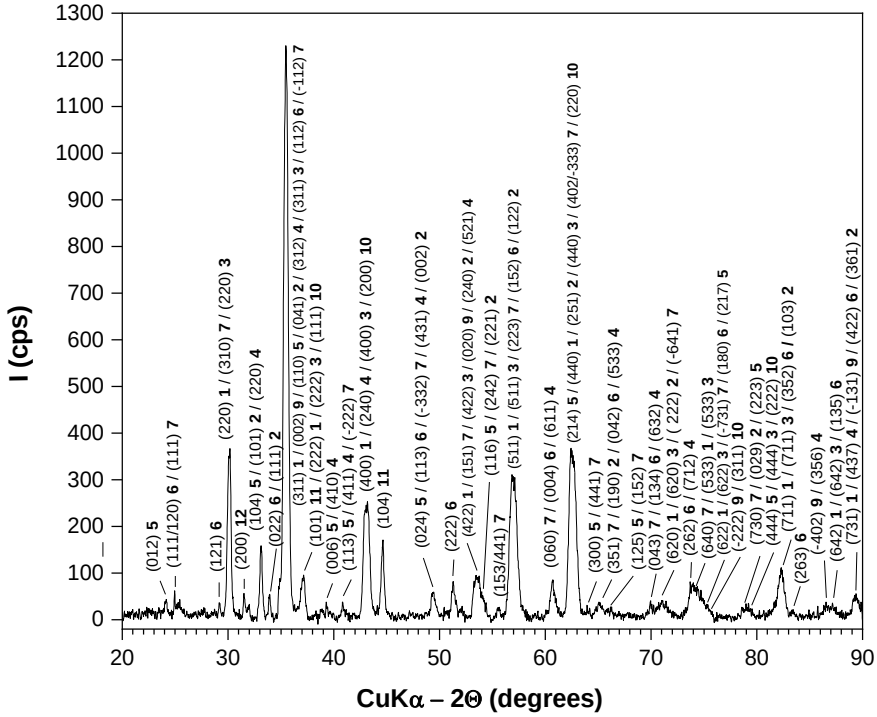


Figure 8. Diffractogram with identified phases of the residual layer on the substrate of AISI 4140 steel oxidized for 20 min at an isothermal temperature of 1000 °C in atmospheric air, with subsequent air cooling.

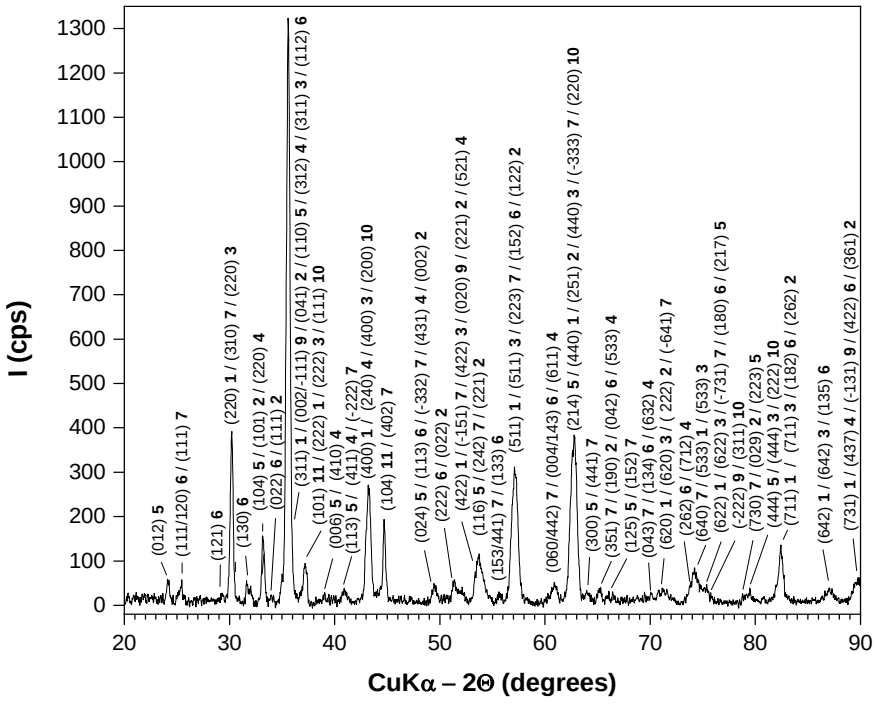


Figure 9. Diffractogram with identified phases of the residual layer on the substrate of AISI 4140 steel oxidized for 40 min at an isothermal temperature of 1000 °C in atmospheric air, with subsequent air cooling.

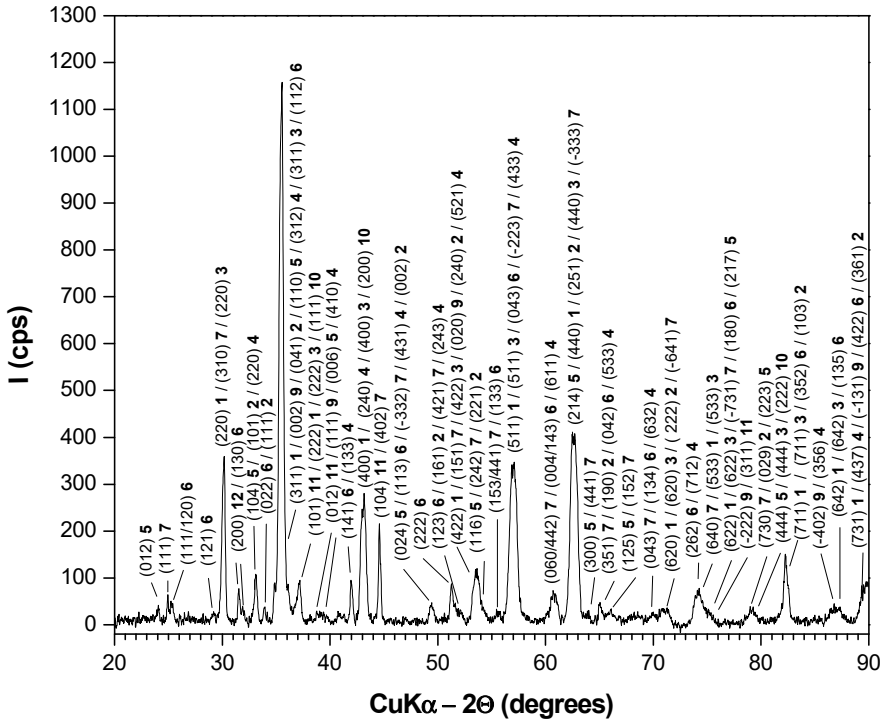


Figure 10. Diffractogram with identified phases of the residual layer on the substrate of AISI 4140 steel oxidized for 60 min at an isothermal temperature of 1000 °C in atmospheric air, with subsequent air cooling.

Figures 8–10 clearly show that oxides are formed from all the alloying elements present in AISI 4140 steel. However, there are three main phases. The predominant phases are Fe_3O_4, $FeCr_2O_4$ and Fe_2O_3.

The residual oxide layer on the substrate is predominantly Fe_3O_4, as evidenced by the high intensity of its characteristic crystallographic peaks, particularly those corresponding to the (311), (400), (220), (511) and (440) planes. The presence of Fe_2O_3 was confirmed by strong peaks associated with the (214) and (104) planes.

As with the inner layer, the most prominent peak for Fe_3O_4 is the (311) plane (IR = 100%). This indicates a random crystallographic orientation with respect to the substrate surface, in contrast to the other phases which show a preferential orientation with respect to the substrate surface.

In addition to the previously identified phases, the presence of Fe_2SiO_4, $FeSiO_3$, MoO_3 and Mn_2O_3 is also indicated by several low-intensity and/or broad peaks, together with contributions from other minor oxides.

It is important to note that the residual oxide layer on the substrate in Figures 8–10 has broader peaks compared to those of the outer and inner layers. This clearly indicates a higher concentration of phases within the residual oxide layer on the substrate, with their diffraction peaks clustered closely together due to similar angular positions. Furthermore, the increased number of peaks observed in the residual oxide layer on the substrate unequivocally indicates that a greater number of crystallographic planes from the existing phases contribute to the overall diffraction pattern.

It is evident that, as with the inner layer, the residual oxide layer on the substrate exhibits peaks of lower absolute intensity in Figures 8–10.

3.3. Superficial Analysis of Oxides

Figures 11 and 12 show scanning electron microscopy (SEM) images of the surface oxide layer at 500× and 2000× magnification, respectively. It is evident that the Fe_2O_3 layer is not flat and that the height of its crystallites increases with oxidation time, resulting in larger crystallite tips. Our analysis of the AISI 4140 steel surfaces oxidised at different

exposure times revealed complete coverage by the oxide layer. This clearly demonstrates that the rate of oxidation at 1000 °C is high. Furthermore, the layers were free of any longitudinal cracks on their surfaces.

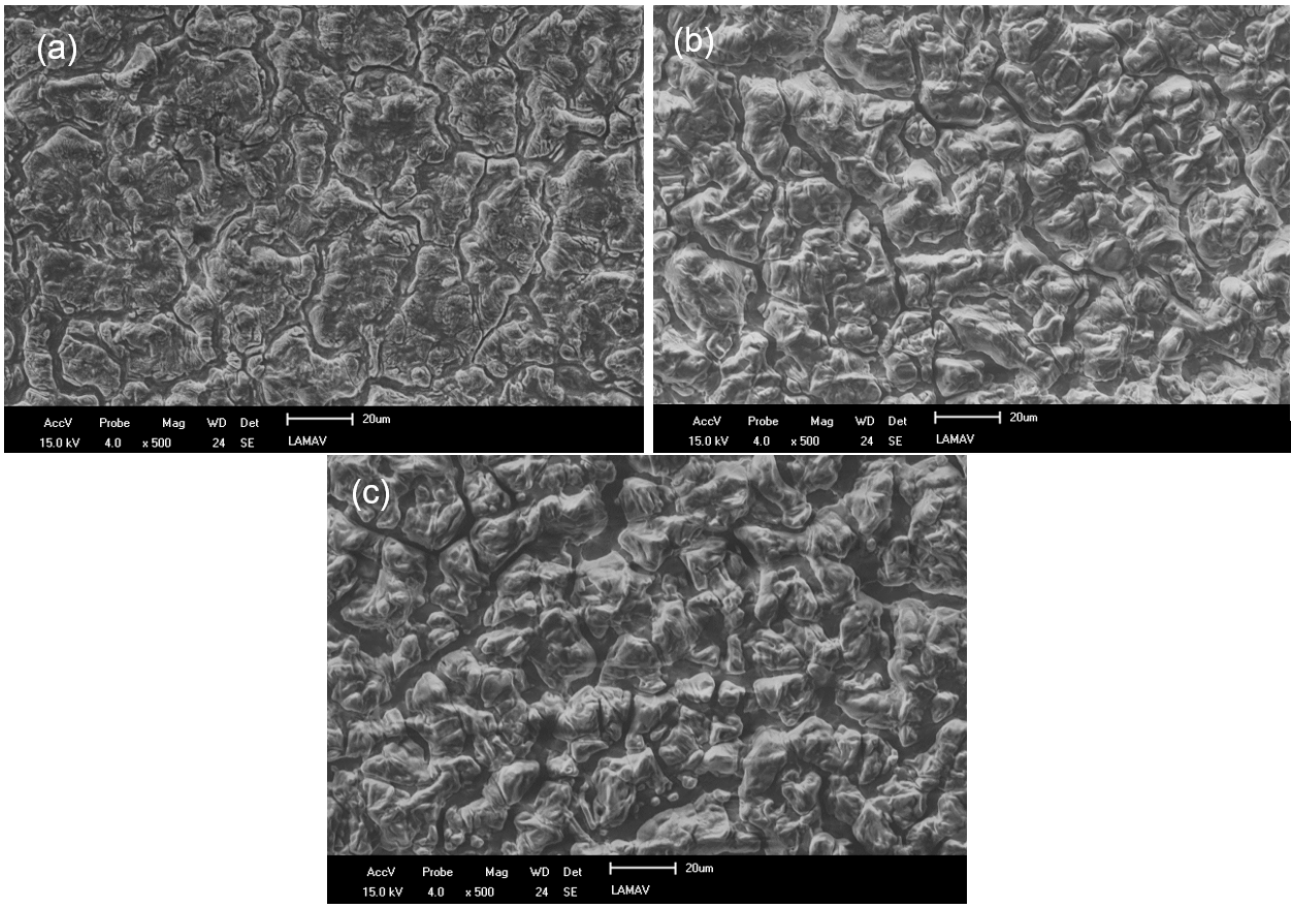


Figure 11. SEM micrograph of the surface oxide layer of AISI 4140 steel oxidized at an isothermal temperature of 1000 °C in atmospheric air for the following times: (**a**) 20 min; (**b**) 40 min; (**c**) 60 min. Magnification: 500×.

The non-planar morphology of the Fe_2O_3 layer is a direct result of the generation and release of stresses within the oxide film, which ultimately leads to flaking. As Song et al. [30] have stated, oxide film stresses can be categorised into two main types: growth stresses and thermal stresses. Growth stresses are directly related to the Pilling–Bedworth ratio (PBR), which is the ratio of the volume of oxide formed during oxidation to the volume of metal consumed to produce the oxide [31]. Thermal stresses occur during the cooling process of the air until the analysis temperature is reached. The combined effect of stress generation and release inevitably results in the detachment of the oxide film from the substrate, which subsequently leads to the formation of cracks and fissures on the surface. This phenomenon is clearly visible in the rougher surface morphology of the outermost Fe_2O_3 layer. Moon and Lee [32] also made similar observations.

The qualitative analysis clearly shows that the surface crystallites become progressively more refined as the oxidation time increases. This is clearly demonstrated by the formation of new, smaller-diameter crystallites with deeper contours and greater thickness. The refinement of the crystallites is also a result of the presence of Mo in the steel. The presence of Mo in the steel results in the formation of MoO_3, a highly volatile oxide. This oxide causes the refinement of oxide crystallites in a manner similar to that observed with the oxides of C, CO and CO_2, which also generates pores and cracks in the scale. As oxidation time increases, there is a clear tendency towards greater formation of MoO_3,

which intensifies the refining of the crystallites. Crystalline refinement results in enhanced elemental diffusivity throughout the oxide layers, with grain boundaries serving as preferential diffusion paths. This intensifies oxidation. Zhang et al. [33] also documented this phenomenon of grain/crystallite refinement due to Mo.

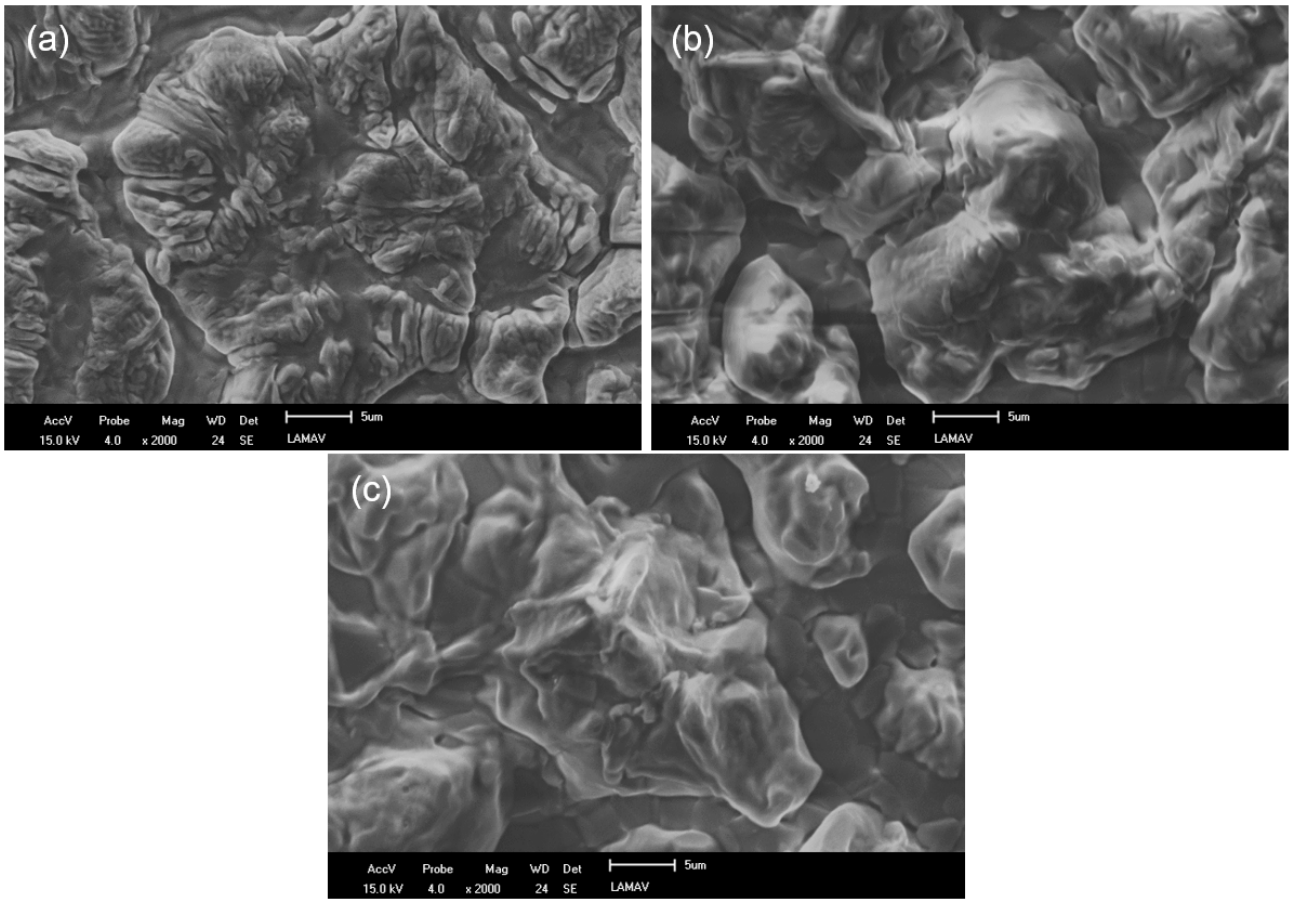


Figure 12. SEM micrograph of the surface oxide layer of AISI 4140 steel oxidized at an isothermal temperature of 1000 °C in atmospheric air for the following times: (**a**) 20 min; (**b**) 40 min; (**c**) 60 min. Magnification: 2000×.

3.4. Cross-Sectional Analysis of Oxides

A cross-sectional analysis definitively revealed the presence of a layered structure in all scales. This structure was consistently composed of Fe_2O_3, Fe_3O_4, FeO and a region adjacent to the metallic substrate that was rich in alloy element oxides.

Figure 13a shows the optical microscopy (OM) image of the AISI 4140 steel that has undergone oxidation over 20 min at 1000 °C, magnified at 200×. At the top, there is a distinct Fe_2O_3 layer, followed by a thicker Fe_3O_4 region. The transformed FeO region lies below this, exhibiting a clear contrast in contrast between the Fe_3O_4 and FeO layers. Contact with the metallic substrate reveals the presence of a region enriched with various alloy element oxides, as previously demonstrated by XRD analysis. The low concentration of alloying elements in 4140 steel definitively impedes the formation of a continuous single-element oxide film, thereby favouring the development of complex oxides with FeO.

Figure 13b presents the optical microscopy (OM) image of the AISI 4140 steel oxidised for 20 min at 1000 °C, with a particular focus on the scale/substrate interface. The region of the alloy element oxides is composed primarily of chromium oxide and FeO ($FeCr_2O_4$). This composition is to be expected, given that chromium is the most abundant alloying element in 4140 steel. This region adheres excellently to the metallic substrate, with no observable detachment. Furthermore, the surface is visually uniform. A region within the

metallic substrate that has undergone internal oxidation is clearly visible beneath the layer of alloy element oxides. This is clearly demonstrated by the presence of areas with varying colour tones.

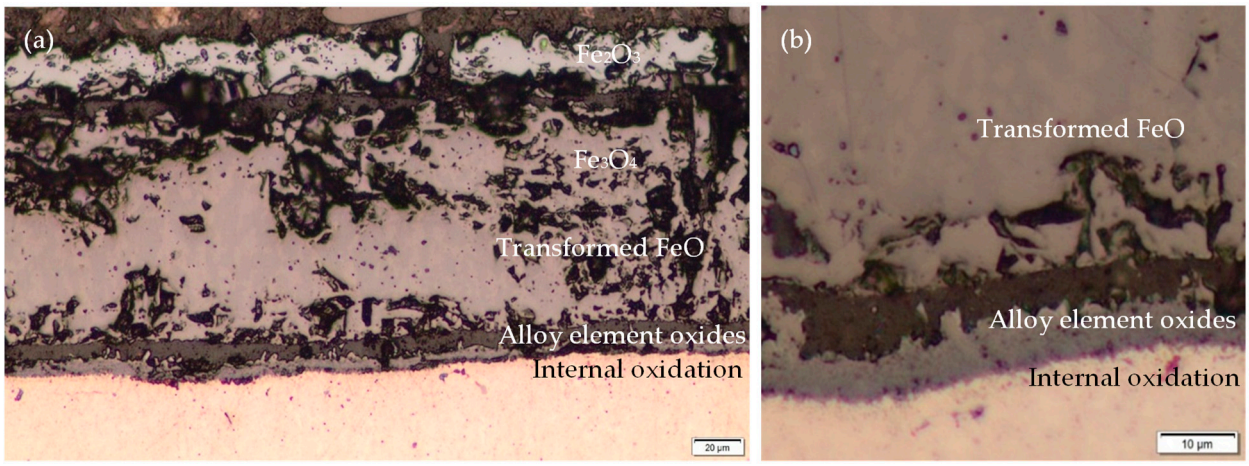


Figure 13. OM of the scale of AISI 4140 steel oxidized for 20 min at an isothermal temperature of 1000 °C in ambient air: (**a**) 200× magnification; (**b**) 500× magnification.

Figure 14a shows the scanning electron microscopy (SEM) image of the AISI 4140 steel oxidised for 20 min at 1000 °C. This is the same region observed in the optical microscopy (OM) Figure 13a. The iron oxide regions are dense, yet they contain cracks. It is evident that the holes are artefacts caused by material removal during the grinding process for sample preparation. In particular, there are clear detachments between the Fe_2O_3 and Fe_3O_4 layers, as well as between the alloy element oxide region and the transformed FeO layer. These detachments are the result of several factors. Firstly, these cracks are the result of growth stresses, which are primarily related to the PBR, as Xu and Gao [34] have discussed. Secondly, these cracks are caused by thermal stresses generated during air cooling. This is in line with the findings of Chaur and Shih [35], who demonstrated that stress generation and release can cause the oxide film to separate from the substrate, leading to surface cracks and fissures. Furthermore, the relationship between the density and crystallinity of the scale phases, as observed by Matlakhov and Robertson et al. [36,37], is a key factor. This is because it leads to detachment between different phases.

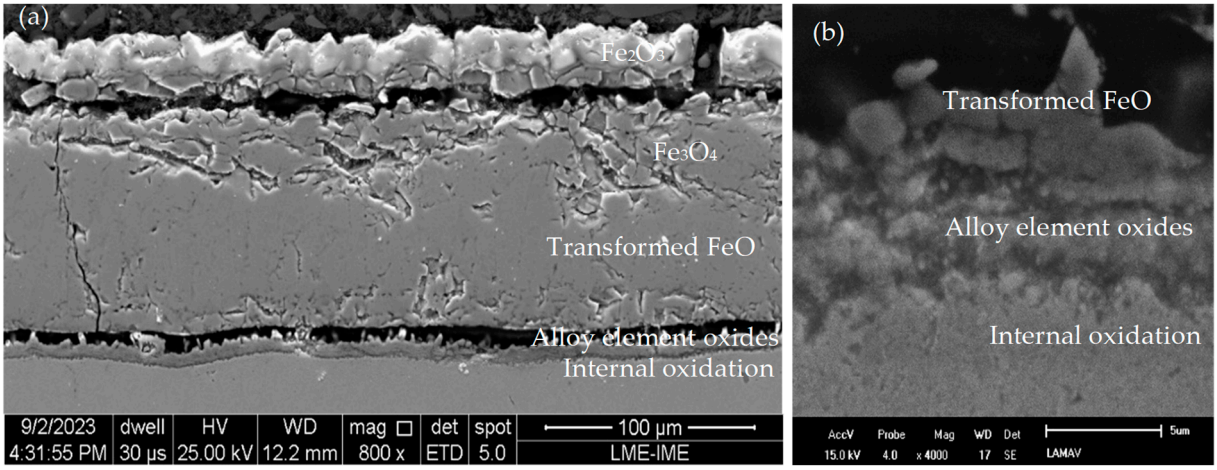


Figure 14. SEM images of the scale of AISI 4140 steel oxidized for 20 min at an isothermal temperature of 1000 °C in atmospheric air: (**a**) 800× magnification; (**b**) 4000× magnification.

Figure 14b shows a higher-magnification scanning electron microscopy (SEM) image of the AISI 4140 steel oxidised for 20 min at 1000 °C. This provides a clear view of the scale/substrate interface. It is evident that the internal oxidation of the substrate has resulted in the formation of porosity in this region due to metal consumption. Furthermore, the FeO layer that underwent transformation exhibits poor adhesion to the layer comprising alloy element oxides.

Figure 15a provides an optical microscopy image of the AISI 4140 steel oxidised for 40 min at 1000 °C. The scale formed at 20 min in Figure 14 is compared with that formed at 40 min, and as oxidation progresses, the number of existing defects increases. Furthermore, the magnetite layer is clearly detaching in certain regions. Furthermore, it is clear that the transformed FeO layer is more detached from the layer of alloy element oxides. Figure 15b shows the scale/substrate region at higher magnification. It is clear that the layer of alloy element oxides begins to detach from the metallic substrate.

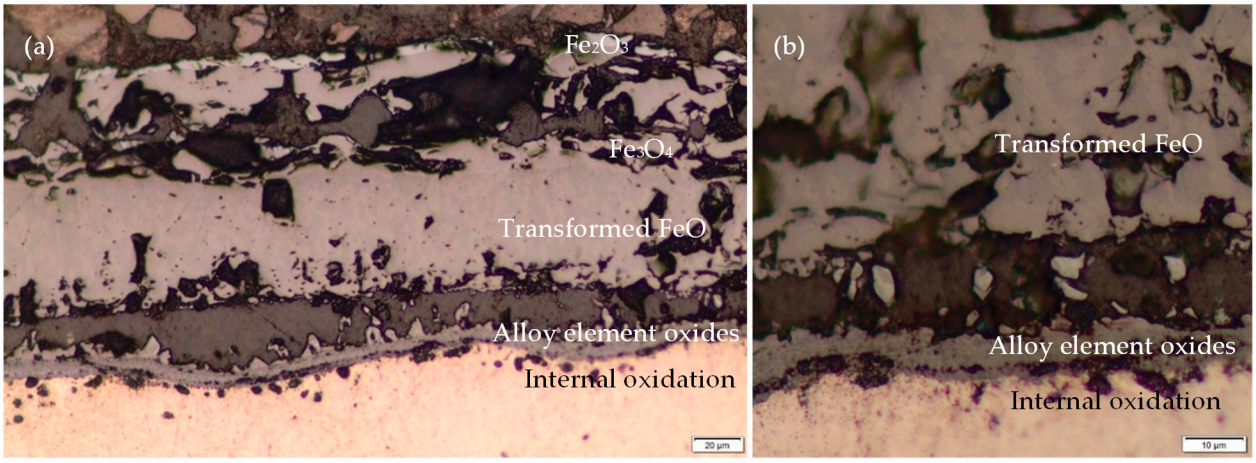


Figure 15. OM images of scale of AISI 4140 steel oxidized for 40 min at an isothermal temperature of 1000 °C in atmospheric air: (**a**) 200× magnification; (**b**) 500× magnification.

Figure 16a shows a detailed SEM microstructure examination of AISI 4140 steel. It is clear that the iron oxide layer has undergone significant alteration following an oxidation process at 1000 °C for 40 min. The previously observed dense regions are now brittle and fractured. Furthermore, Figure 16b presents a higher magnification image of the scale/substrate interface, which clearly shows the detachment of the oxidised alloy element layer from the underlying metallic substrate. Furthermore, the region of internal oxidation and the remaining alloy element oxides are highly porous.

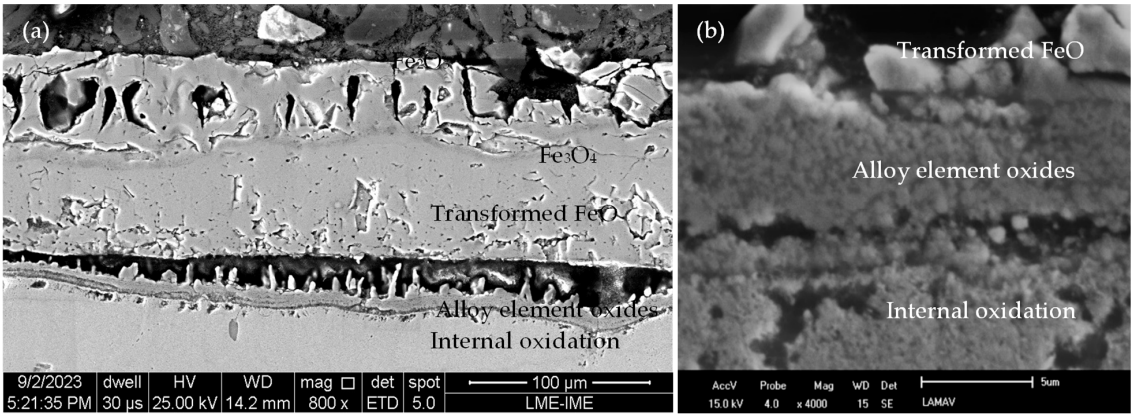


Figure 16. SEM images of the scale of AISI 4140 steel oxidized for 40 min at an isothermal temperature of 1000 °C in atmospheric air: (**a**) 800× magnification, (**b**) 4000× magnification.

Figure 17a presents the optical microscopy (OM) image of the AISI 4140 steel that has been oxidised for 60 min at 1000 °C. It is evident that the number of defects within the scale increases with the duration of the oxidation process. Figure 17b shows a higher magnification view of the scale/substrate interface, which clearly demonstrates a more pronounced detachment of the alloy element oxide layer from the underlying metallic substrate.

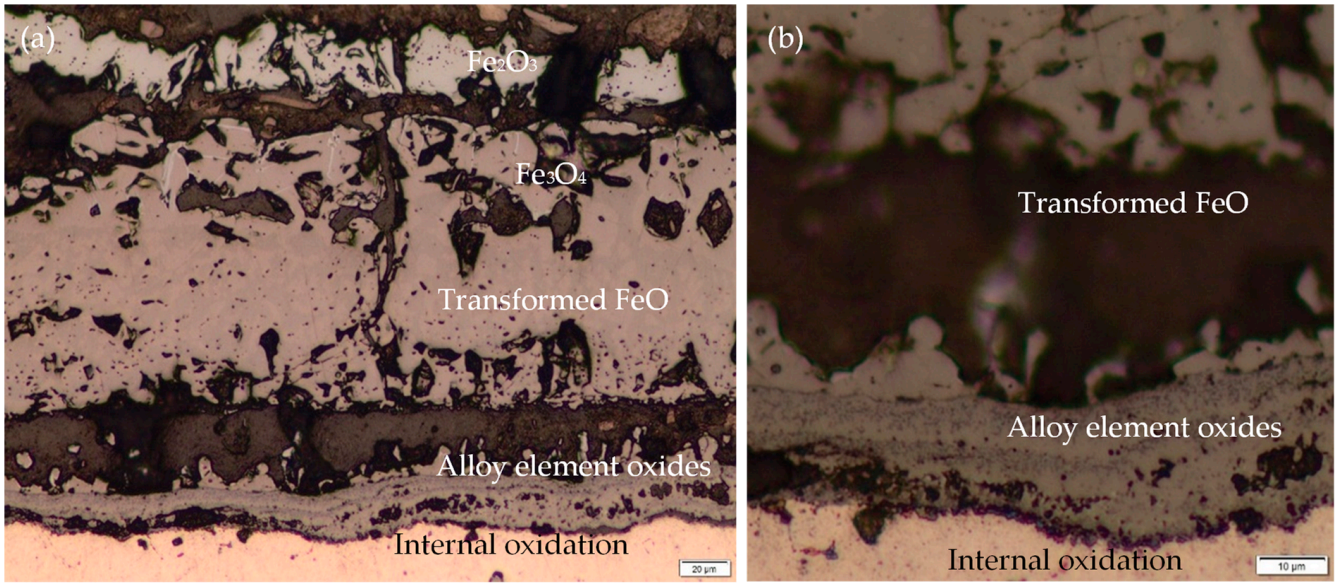


Figure 17. OM images of the scale of AISI 4140 steel oxidized for 60 min at an isothermal temperature of 1000 °C in atmospheric air: (**a**) 200× magnification, (**b**) 500× magnification.

As previously discussed, the region shown in Figure 17 is composed of Fe_3O_4 and transformed FeO, which is highly dense at the 20 min oxidation time. However, the 40 and 60 min oxidation times show a fractured and cracked morphology with a thicker defect layer, resulting in greater separation between the dense layers. The growing scale experiences compressive stress, given that the scale growth follows a parabolic kinetic. This explains the non-compact scale observed at 40 and 60 min. As the number of defects and cracks within the layer increases, $FeCr_2O_4$ inevitably ruptures. As the process continues, the oxidation of Fe increases due to Cr depletion at the substrate surface. As shown by Sadique et al. [22], this results in a significant increase in the oxidation rate after rupture, leading to the formation of more Fe_2O_3, Fe_3O_4 and FeO.

Figure 18a presents the SEM image of AISI 4140 steel oxidised for 60 min at 1000 °C in the same region previously observed in the optical microscope (OM) image displayed in Figure 17. The Fe_2O_3 layer is completely separated from the underlying Fe_3O_4 layer. Furthermore, the scale is clearly cracked throughout, with a highly porous transformed FeO layer. Furthermore, it is evident that the layer of alloy element oxides becomes increasingly detached from the metallic substrate as oxidation time increases. Figure 18b shows the scale/substrate interface at a higher magnification. It is evident that the alloy element oxide layer is detached from the metallic substrate, and that there is also detachment within the alloy element oxide layer itself, in addition to the presence of a region of high porosity.

Figure 19 displays the SEM image of the AISI 4140 steel oxidised for 60 min at 1000 °C. This image clearly shows the interface between the transformed FeO layer and the layer of alloy element oxides. It is evident that the detachment between these layers is incomplete and that the surfaces of both layers are uneven, which hinders their complete adhesion. In some areas, the layers remain connected, while in others, there is a clear separation.

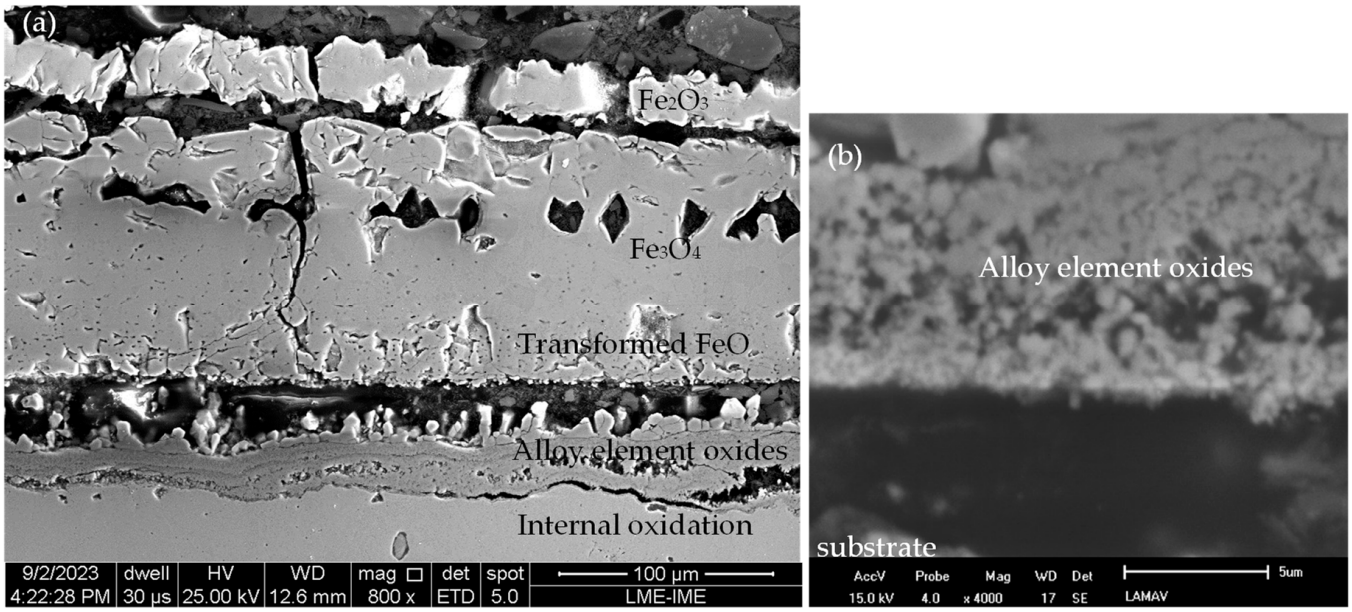


Figure 18. SEM images of the scale of AISI 4140 steel oxidized for 60 min at an isothermal temperature of 1000 °C in atmospheric air: (**a**) 800× magnification, (**b**) 4000× magnification.

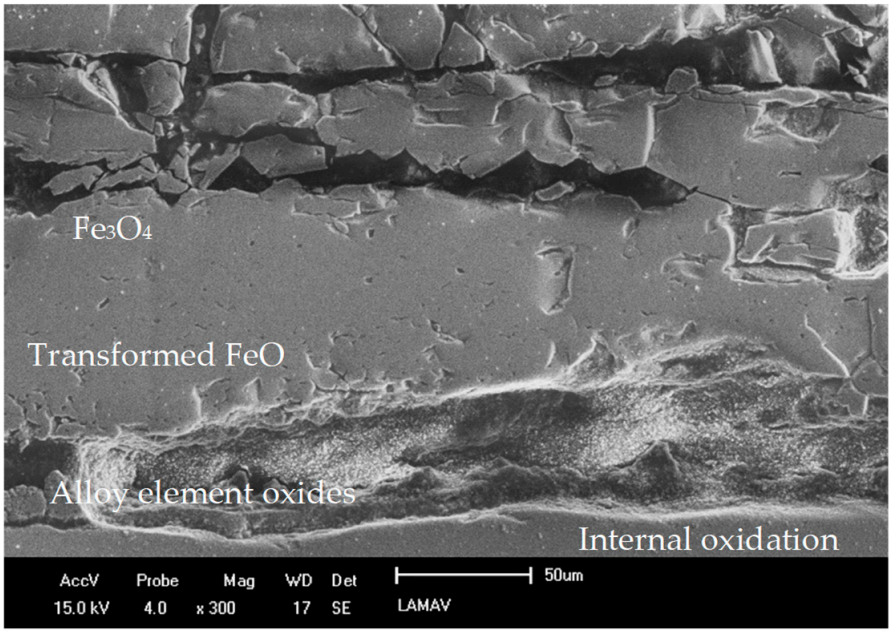


Figure 19. SEM image of the scale formed on AISI 4140 steel oxidized for 60 min at 1000 °C in atmospheric air (300× magnification).

From Table 4 and Figure 20, it can be seen that the scale thickness increases with increasing oxidation time.

Table 4. Scale thickness in µm of 4140 steel at 1000 °C as a function of time exposed to oxidation in atmospheric air.

	20 min	**40 min**	**60 min**
Mass	133.8068	146.4348	197.3375
Standard Deviation	6.4364	14.1468	20.1042

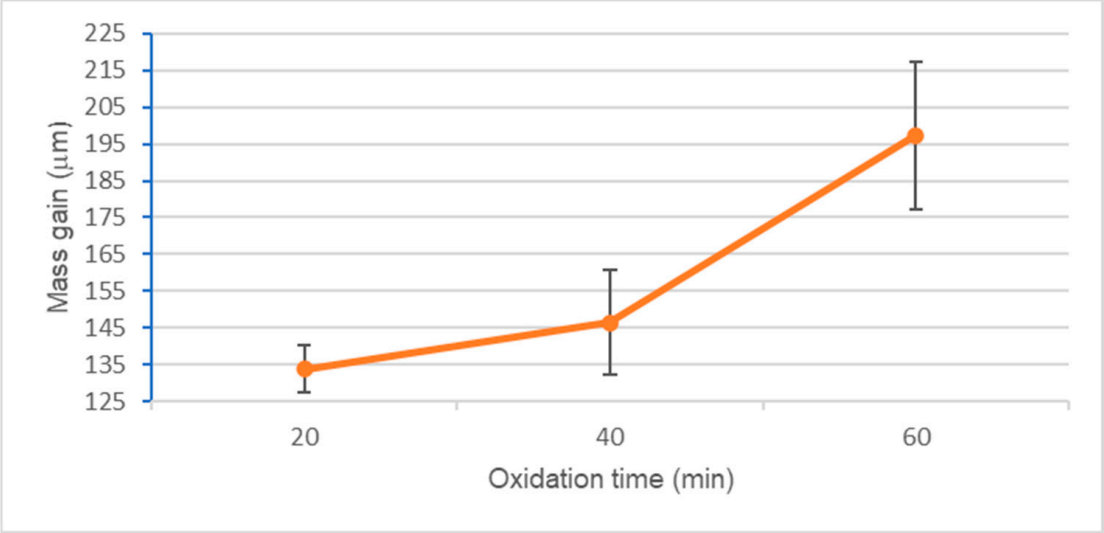


Figure 20. Scale thickness in µm of 4140 steel at 1000 °C as a function of time exposed to oxidation in atmospheric air.

Through the images shown in Figure 21a–c of the cross-sectional micrographs of the 4140 steel at oxidation times of 20, 40 and 60 min, respectively, it is possible to confirm what was presented in Table 4 and Figure 20. The scale increases in thickness with the increase in oxidation time.

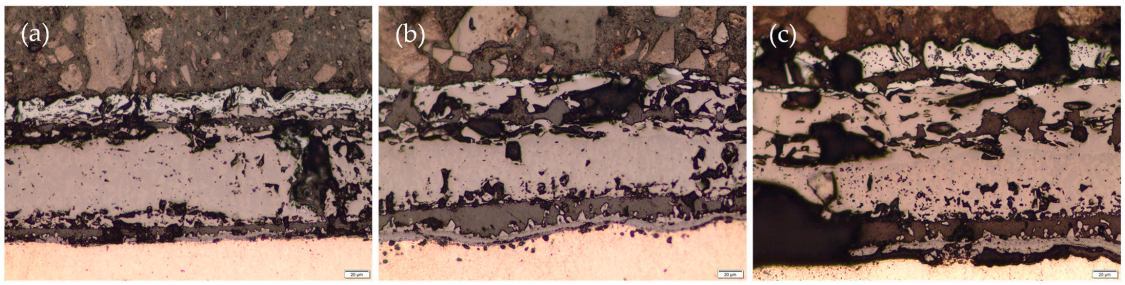


Figure 21. Comparison of scale thickness at 1000 °C, in atmospheric air, as a function of exposure time to oxidation, of 4140 steel at the following times: (**a**) 20 min; (**b**) 40 min; (**c**) 60 min. Magnification 200×.

The images of the cross-sectional micrographs of the 4140 steel at oxidation times of 20, 40 and 60 min are shown in Figure 21a–c, respectively, confirm the data presented in Table 4 and Figure 20. The scale increases in thickness as the oxidation time increases.

3.5. Chemical Analysis

Table 5 presents the results of EDS mapping, which reveal the distribution of elements across the cross-section of the AISI 4140 steel oxidised for 20, 40, and 60 min at 1000 °C.

Table 5. EDS elemental maps of the cross-section of 4140 steel oxidized at 1000 °C.

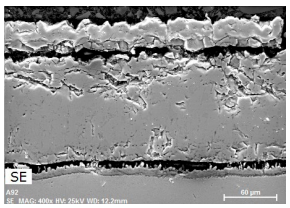
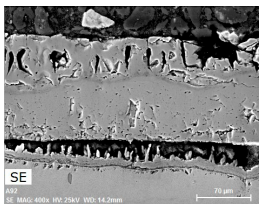
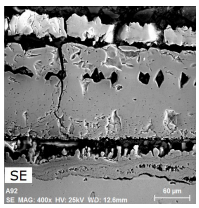
Alloy Element	20 min	40 min	60 min
SE			

Table 5. *Cont.*

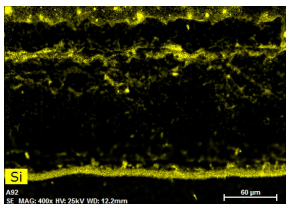
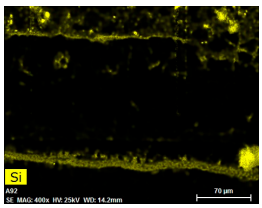
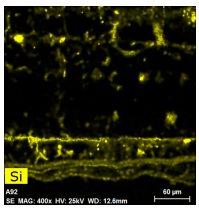
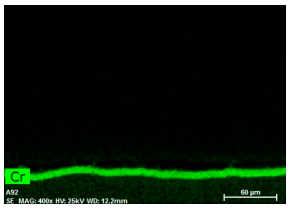
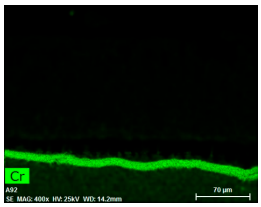
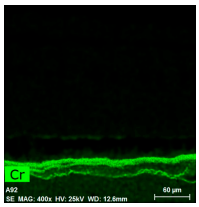
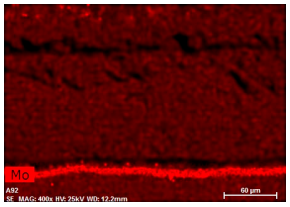
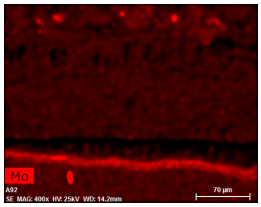
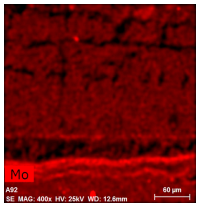
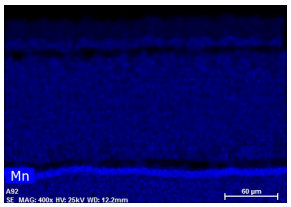
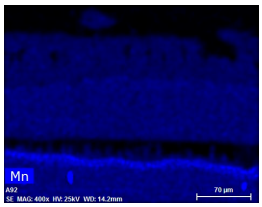
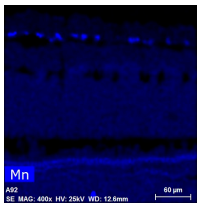
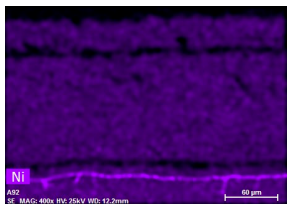
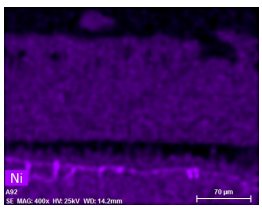
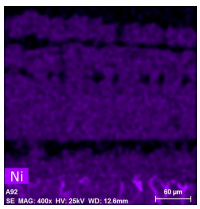
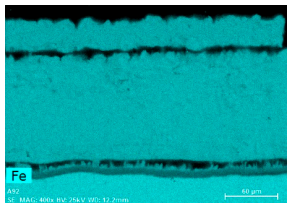
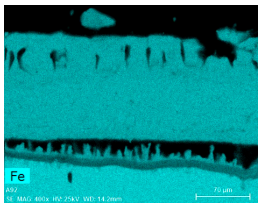
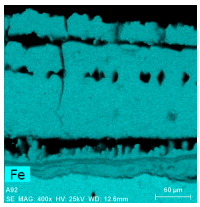
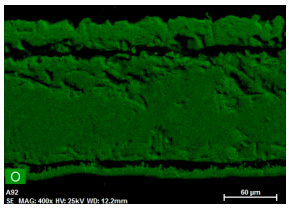
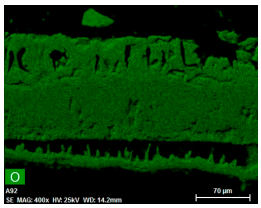
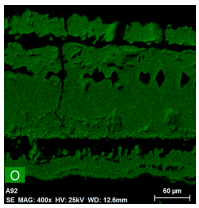
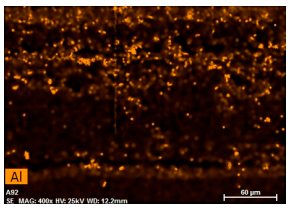
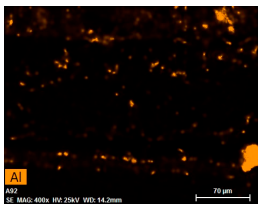
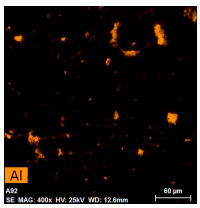
Alloy Element	20 min	40 min	60 min
Si			
Cr			
Mo			
Mn			
Ni			
Fe			
O			

Table 5. *Cont.*

Alloy Element	20 min	40 min	60 min
Al			

Significant quantities of silicon are present near the substrate. This can be attributed to the formation of $FeSiO_3$ and Fe_2SiO_4, which have already been discussed and confirmed by the XRD results. Furthermore, it is likely that some silicon originated from SiC contamination during the grinding process, as evidenced by its concentration in scale defects and voids.

The elevated aluminium concentration can be attributed to the potential contamination of alumina from the polishing process. Similarly, aluminium is concentrated in scale defects.

Oxygen is found in higher concentrations in the outer region of the scale, with a subsequent decrease towards the substrate. This is in line with the higher oxygen content in Fe_2O_3 compared to Fe_3O_4. The metallic substrate is predominantly composed of iron.

The alloying elements Cr, Mo and Mn are essential for the oxidation process, with the highest concentrations occurring in the vicinity of the substrate. These elements, in conjunction with Si, formed a clearly delineated layer comprising the mixed oxides of the aforementioned elements. This layer is the reason why 4140 steel resists oxidation. It is clear that chromium is the primary factor driving the formation of this thick, alloy-rich layer. As the alloying element with the highest percentage in the 4140 steel's chemical composition, chromium is the key factor in determining the kinetic and mechanism of oxide film formation on the substrate. Furthermore, the film contains oxides of other alloying elements.

It is clear from the clustering of these elements that the formed oxides are insufficient to create a complete and dense protective film. These observations are in line with those of Xu et al. (2013) [38], who correctly noted that low-quantity alloying element oxides tend to form complex oxides with FeO in the same region.

It is evident that manganese dioxide (MnO_2) accumulates at the interface between iron (II, III) oxide (Fe_2O_3) and iron (III) oxide (Fe_3O_4), while a minor quantity of molybdenum trioxide (MoO_3) is present in the outermost layer of Fe_2O_3.

The Ni, present in a low percentage, forms an irregular oxide layer in the vicinity of the substrate at shorter oxidation times. As the oxidation time increases, NiO is observed to penetrate the substrate through transgranular corrosion of austenite, as reported by Zhang et al. [39].

It is evident that over time, there is a reduction in the concentration of alloying elements in the vicinity of the substrate. As the thickness of the alloy oxide layer increases over time, these elements disperse.

Figure 22 illustrates the EDS analysis of the AISI 4140 steel that had been oxidised for 20 min at eight different locations on the concentration profile (CP). Table 6 shows the corresponding chemical composition results.

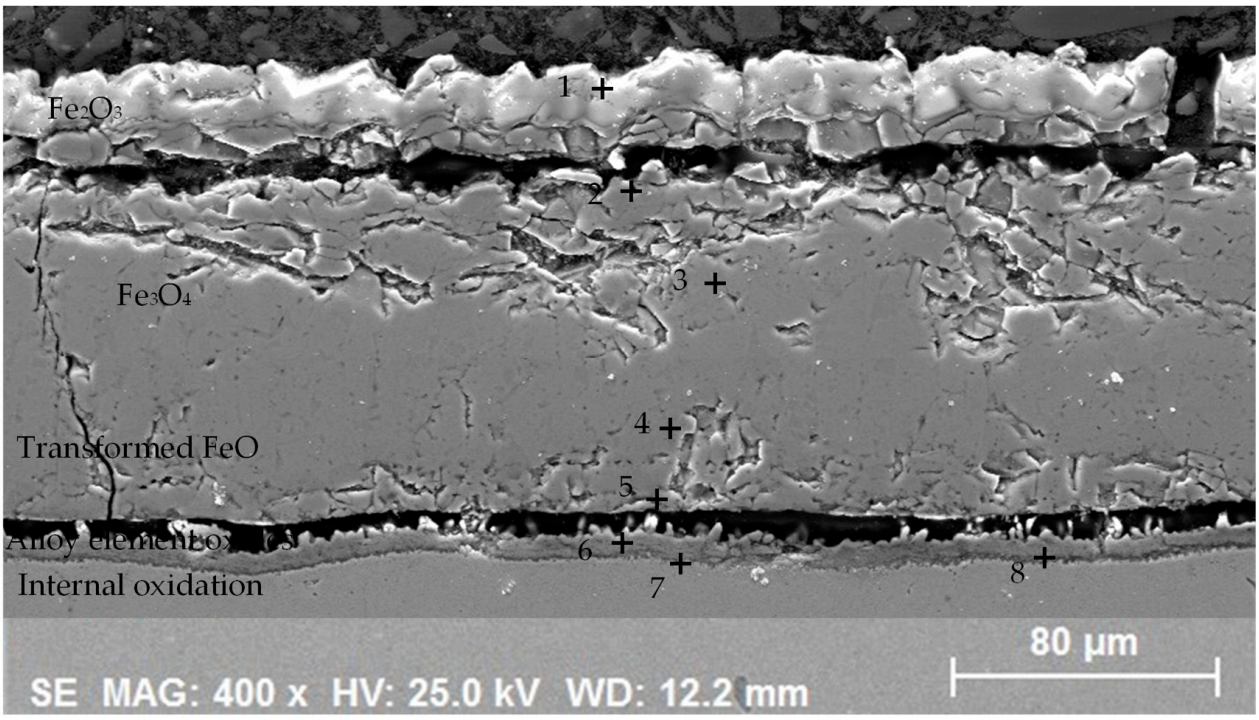


Figure 22. Cross-Section and EDS Analysis of AISI 4140 Steel Oxidized (20 min, 1000 °C, Air).

Table 6. Elemental Composition (wt%) of AISI 4140 Steel Oxidized for 20 min at 1000 °C in Air (EDS Analysis).

Point Position	O	Fe	Si	Mn	Al	Mo	Ni	Cr	Cu
1	45.26	53.88	0.09	0.37	0.28	-	0.07	0.05	-
2	43.37	55.51	0.12	0.72	0.21	-	0.06	0.01	-
3	36.15	62.65	0.09	1.00	0.05	-	0.04	0.04	-
4	36.19	62.34	0.14	1.01	0.07	0.06	0.04	0.10	0.05
5	42.18	56.05	0.10	0.99	0.12	-	0.08	0.45	0.04
6	42.25	36.50	4.04	1.00	0.17	0.92	0.06	14.68	0.37
8	37.75	32.73	6.49	1.45	-	0.25	0.63	17.71	2.98
7	2.04	91.67	0.26	1.38	0.04	-	0.55	2.23	1.82

The EDS analysis clearly indicates a reduction in oxygen content and an increase in Fe content as the analysis is conducted from the outer region, which is dominated by Fe_2O_3, towards the substrate point 4 and beyond. This region undoubtedly contains Fe_3O_4. Therefore, the presence of various iron oxides, as also confirmed by the XRD analysis, can be confirmed.

It can be observed that, up to point 4, the region is mainly concentrated with a Fe_2O_3 layer, followed by Fe_3O_4. As points approach the substrate, the oxygen content decreases and the Fe content increases.

At points 5 and 6, the oxygen content increases once more while the Fe content decreases. These points correspond to the transformed FeO and the region of alloying element oxides, respectively.

This finding is consistent with the higher concentration of alloying element oxides observed in this region. Silicon is present throughout the scale in low percentages. However, it is clear that points 6 and 8 show a significant increase in Si. This is undoubtedly due to the formation of Fe_2SiO_4, a phase that has been confirmed by X-ray diffraction analysis. All the alloying elements are present in this region, with chromium being the most abundant. The formation of alloying element oxides undoubtedly occurs below the original interface, which proves that oxygen diffusion is a pivotal factor in these reactions.

Point 7 definitively marks the region of internal oxidation. It is clear that all elements, except for molybdenum, are involved in this process. The most prevalent elements involved are chromium, copper, and manganese, with an increase in manganese content observed as points approach the substrate.

These findings are in accordance with those previously reported by Hao et al. [40]. Similarly, the formation of a cluster of alloying elements near the substrate was observed, as confirmed by XRD, which definitively displayed the presence of complex oxides. The authors do not explicitly state this, but their results clearly show a decrease in oxygen and an increase in iron content as the metallic substrate gets closer. Furthermore, they observed a clear increase in oxygen content in the region containing these complex oxide clusters.

Figure 23 presents the EDS analysis of the AISI 4140 steel oxidised for 40 min at 1000 °C, conducted at eight positions on the cross-section. Table 7 provides the results of the chemical composition analysis.

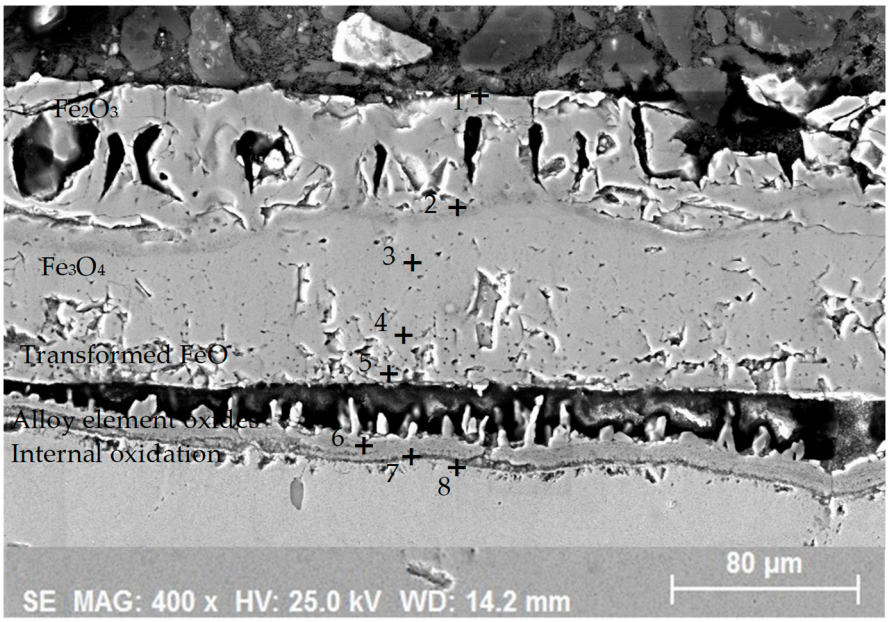


Figure 23. Cross-sectional and EDS analysis at different positions of AISI 4140 steel oxidized (40 min, 1000 °C, air).

Table 7. Elemental Composition (wt%) of AISI 4140 Steel Oxidized for 40 min at 1000 °C in Air (EDS Analysis).

Point Position	O	Fe	Si	Mn	Al	Mo	Ni	Cr	Cu
1	47.40	51.42	0.37	0.64	-	-	0.08	0.02	0.05
2	40.57	57.83	0.14	1.39	-	-	0.04	-	0.02
3	37.98	60.73	0.04	1.12	-	-	0.02	0.08	0.03
4	36.76	61.75	0.10	1.13	-	-	0.04	0.05	0.05
5	37.58	59.59	0.13	0.81	0.11	0.05	0.09	0.69	0.94
6	45.63	36.08	3.62	0.97	-	0.62	0.04	12.95	0.09
7	37.71	37.87	5.06	1.64	0.50	0.51	0.52	12.96	3.23
8	0.90	91.74	0.15	1.09	0.11	0.04	2.38	1.60	1.99

The 40 min and 20 min oxidation outcomes are distinctly different, as shown in point 8, which represents the region of internal oxidation. Table 7 clearly shows all elements are involved in the internal oxidation process, with Ni, Cu, Cr, and Mn being the most prevalent. The point analysis results align with the map analysis trend. As the oxidation time increases, there is a clear trend towards a greater prevalence of Ni in the internal oxidation process.

Figure 24 presents the EDS analysis of the AISI 4140 steel oxidised for 60 min at 1000 °C. The analysis was conducted at eight positions on the cross-section. Table 8 outlines the chemical composition analysis results.

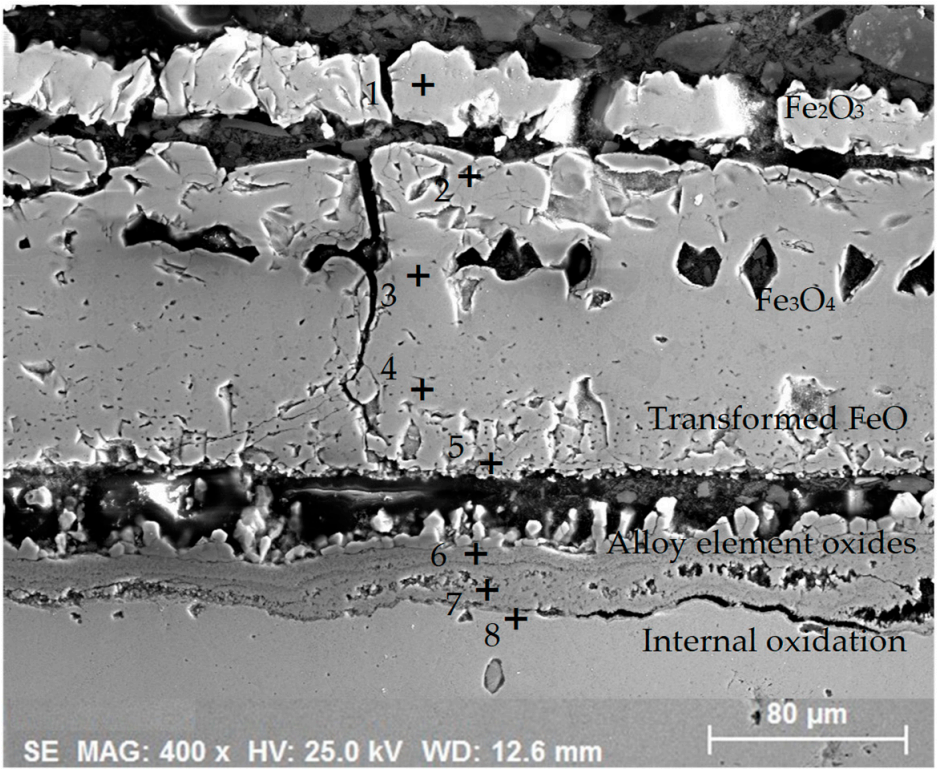


Figure 24. Cross-sectional and EDS analysis at different positions of AISI 4140 steel oxidized (60 min, 1000 °C, air).

Table 8. Elemental Composition (wt%) of AISI 4140 Steel Oxidized for 60 min at 1000 °C in Air (EDS Analysis).

Point Position	O	Fe	Si	Mn	Al	Mo	Ni	Cr	Cu
1	43.60	55.77	0.08	0.44	0.06	-	0.08	0.03	0.01
2	51.99	47.35	0.09	0.44	0.07	-	0.06	-	-
3	36.32	62.20	0.08	1.17	0.07	0.02	0.03	0.05	0.05
4	36.81	61.72	0.13	1.13	-	0.01	0.07	0.10	0.04
5	42.46	55.69	0.22	0.78	0.19	0.02	0.03	0.38	0.24
6	37.49	45.01	2.70	0.94	0.38	0.38	0.01	12.98	0.10
7	38.91	53.16	2.10	0.94	0.24	-	0.12	4.48	0.04
8	0.19	96.45	0.36	1.43	0.07	0.04	0.05	1.18	0.22

As can be seen, the results are in line with those previously discussed in relation to the sample oxidized for 20 and 40 min. As with the previous observations, the selected points irrefutably demonstrate that the concentration of oxygen tends to diminish as it approaches the substrate. However, an increase in oxygen content is clearly visible when point analysis is conducted in the vicinity of the layer comprising alloying element oxides.

Regarding point 8, representing the internal oxidation region, it is evident that all elements engage in this process, with Mn, Cr, Si, and Cu playing a predominant role. The selected point did not identify a high Ni content, confirming that its concentration is non-uniform. The map analysis clearly shows that as the oxidation time increases, Ni becomes increasingly involved in internal oxidation.

Furthermore, the percentage of alloying elements is clearly lower at points 6 and 7 than at the other instances within this same region. This confirms the map analysis results,

which showed that the dispersion of alloying elements increases with the thickness of the layer of alloying element oxides over time.

In future investigations, it will be important to study in situ these complex processes of oxidation at high temperatures using the Raman spectroscopy method.

4. Conclusions

This study presents the findings derived from the analysis of three oxide layers formed on the surface of AISI 4140 steel subjected to 1000 °C for 20, 40 and 60 min. This is the first time such a cross-section has been analysed, and the results are clear. The following conclusions can be drawn:

- The oxide layers exhibited a composition of Fe_2O_3, Fe_3O_4, and FeO, with the formation of the layer being attributed to a cluster of alloying element oxides, with a greater influence exerted by Fe and $FeCr_2O_4$.
- The outermost layer is primarily composed of Fe_2O_3, exhibiting a strong preferential crystallographic orientation relative to the steel substrate surface.
- The inner layer is dominated by Fe_3O_4, exhibiting no preferential crystallographic orientation relative to the steel substrate surface.
- Wüstite is present in the form of complex oxides with alloying element oxides.
- The substrate layer also features Fe_3O_4 as the main phase, which is likely to have formed from FeO during cooling. This phase lacks preferential crystallographic orientation relative to the steel substrate surface.
- The participation of alloying element oxides in the scale layers is approximately proportional to the concentrations of these elements in the alloy.
- The AISI 4140 steel, at all oxidation times, exhibited complete coverage of the surface by oxide layers, with no evidence of longitudinal cracking.
- The crystallites of Fe_2O_3 in the outer layer demonstrate a tendency for increased height as the oxidation time is prolonged.
- The promotion of crystallite refinement on the scale surface by Mo occurs in a manner which is intensified with increasing oxidation time.
- The scale thickness and the incidence of defects also increased with the extension of the oxidation time.
- The layer of alloying element oxides exhibited poor adhesion to the steel substrate, and the alloying element oxides present in this layer had poor adhesion to each other. This weak adhesion was further intensified at 60 min, which in turn promoted the formation of a thicker oxide scale.
- The most abundant alloying element in carbon steel, chromium, plays a pivotal role in determining the kinetics and mechanism of oxide formation at the substrate interface. Nevertheless, the presence of the $FeCr_2O_4$ phase is likely to contribute to the observed poor adhesion of this layer.
- The alloying elements present in low quantities (Ni, Mo, Mn, Si, Cr) were unable to form their own continuous oxide films. Conversely, these elements are dispersed throughout all scale layers, with higher concentrations observed in the inner layer in proximity to the steel substrate.
- As the oxidation time increased up to 60 min, the oxide layer in contact with the steel substrate exhibited a corresponding increase in thickness. During this process, the oxides of alloying elements such as nickel, molybdenum, chromium, manganese, and silicon displayed a tendency to disperse within the layer.

Author Contributions: Conceptualization, M.O.C. and L.A.M.; Methodology, M.O.C. and L.A.M.; Software, M.O.C., L.A.M. and R.S.T.M.; Validation, L.A.M., S.N.M., R.S.T.M. and N.A.P.; Formal analysis, M.O.C.; Investigation, M.O.C.; Resources, M.O.C.; Data curation, M.O.C.; Writing—original draft, M.O.C.; Writing—review & editing, L.A.M., S.N.M., R.S.T.M. and N.A.P.; Visualization, M.O.C.; Supervision, L.A.M.; Project administration, M.O.C. and L.A.M.; Funding acquisition, M.O.C., L.A.M., S.N.M., R.S.T.M. and N.A.P. All authors have read and agreed to the published version of the manuscript.

Funding: This research received no external funding.

Data Availability Statement: The original contributions presented in the study are included in the article, further inquiries can be directed to the corresponding author.

Conflicts of Interest: The authors declare no conflict of interest.

References

1. Zhang, L.; Thomas, B.G. State of the art in the control of inclusions during steel ingot casting. *Metall. Mater. Trans. B* **2006**, *37*, 733–761. [CrossRef]
2. Zhong, M.; Webler, B.A. High temperature oxidation behaviors of steels at initial stages in air. *Corros. Sci.* **2024**, *229*, 111838. [CrossRef]
3. Martín, M.I.; López, F.A.; Torralba, J.M. Production of sponge iron powder by reduction of rolling mill scale. *Ironmak. Steelmak.* **2012**, *39*, 155–162. [CrossRef]
4. Weihua, S.; Tieu, A.K.; Zhengyi, J.; Cheng, L. High temperature oxide scale characteristics of low carbon steel in hot rolling. *Mater. Process. Technol.* **2004**, *155*, 1307–1312. [CrossRef]
5. Carvalho, M.O.; Matlakhova, L.A.; Monteiro, S.N. Influence of chemical composition on the hot oxidation of carbon steel—A review. *J. Eng. Res.* **2024**, *4*, 1–16. [CrossRef]
6. Basabe, V.V.; Szpunar, J.A. Effect of O_2 in heating atmosphere on hydraulic descaling in hot rolling of low carbon steel. *ISIJ Int.* **2008**, *48*, 467–474. [CrossRef]
7. Bhattacharya, R.; Jha, G.; Kundu, S.; Shankar, R.; Gope, N. Influence of cooling rate on the structure and formation of oxide scale in low carbon steel wire rods during hot rolling. *Surf. Coat.* **2006**, *201*, 526–532. [CrossRef]
8. Yuan, Q.; Xu, G.; Zhou, M.; He, B. The effect of the Si content on the morphology and amount of Fe_2SiO_4 in low carbon steels. *Metals* **2016**, *6*, 94. [CrossRef]
9. Genève, D.; Rouxel, D.; Pigeat, P.; Weber, B.; Confente, M. Surface composition modification of high-carbon low-alloy steels oxidized at high temperature in air. *Appl. Surf. Sci.* **2008**, *254*, 5348–5358. [CrossRef]
10. Wu, Q.; Liu, Y.; Zhang, Z.; Qi, Y.; Zhang, C.; Zheng, H.; Xu, Y. Oxidation behavior and high-temperature tensile properties of Fe-9Cr-(Mo, Mo/Ni) alloys. *Corros. Sci.* **2021**, *181*, 109243. [CrossRef]
11. Yuan, Q.; Xu, G.; Liang, W.; Zhou, M.; Hu, H. Effects of Oxygen Concentration on the Passivation of Si-Containing Steel during High-Temperature Oxidation. *Corros. Rev.* **2018**, *36*, 385–393. [CrossRef]
12. Li, H.; Zhao, C.; Yan, T.; Ding, C.; Zhang, H.; Jiang, F. Properties of high temperature oxidation of heat-resistant steel with aluminum and copper. *Mater. Sci.* **2019**, *25*, 394–400. [CrossRef]
13. Nebol'sin, V.A.; Johansson, J.; Suyatin, D.B.; Spiridonov, B.A. Thermodynamics of oxidation and reduction during the growth of metal catalyzed silicon nanowires. *J. Cryst. Growth.* **2019**, *505*, 52–58. [CrossRef]
14. Genève, D.; Rouxel, D.; Weber, B.; Confente, M. Segregation across the metal/oxide interface occurring during oxidation at high temperatures of diluted iron-based alloys. *Mater. Sci. Eng. A* **2006**, *435*, 1–11. [CrossRef]
15. Hanesch, M. Raman spectroscopy of iron oxides and (oxy) hydroxides at low laser power and possible applications in environmental magnetic studies. *Geophys. J. Int.* **2009**, *177*, 941–948. [CrossRef]
16. Rossignol, S.; Gérard, F.; Mesnard, D.; Kappenstein, C.; Duprez, D. Structural changes of Ce–Pr–O oxides in hydrogen: A study by in situ X-ray diffraction and Raman spectroscopy. *J. Mater. Chem.* **2003**, *13*, 3017–3020. [CrossRef]
17. Mougin, J.; Le Bihan, T.; Lucazeau, G. High-pressure study of Cr_2O_3 obtained by high-temperature oxidation by X-ray diffraction and Raman spectroscopy. *J. Phys. Chem. Solids* **2001**, *62*, 553–563. [CrossRef]
18. Böhme, N.; Hauke, K.; Dohrn, M.; Neuroth, M.; Geisler, T. High-temperature phase transformations of hydroxylapatite and the formation of silicocarnotite in the hydroxylapatite–quartz–lime system studied in situ and in operando by Raman spectroscopy. *J. Mater. Sci.* **2022**, *57*, 15239–15266. [CrossRef]
19. Zhang, B.; Tekle, H.; O'Malley, R.J.; Smith, J.D.; Gerald, R.E.; Huang, J. In situ high-temperature Raman spectroscopy via a remote fiber-optic Raman probe. *IEEE Trans. Instrum. Meas.* **2023**, *72*, 1–8. [CrossRef]
20. Slotznick, S.P.; Shim, S.H. In situ Raman spectroscopy measurements of $MgAl_2O_4$ spinel up to 1400 C. *Am. Mineral.* **2008**, *93*, 470–476. [CrossRef]
21. Dubiel, S.M.; Zukrowski, J. Kinetics of phase separation, border of miscibility gap in Fe–Cr and limit of Cr solubility in iron at 832 K. *Mater. Charact.* **2019**, *158*, 109937. [CrossRef]
22. Sadique, S.E.; Mollah, A.H.; Islam, M.S.; Ali, M.M.; Megat, M.H.H.; Basri, S. High-Temperature Oxidation Behavior of Iron–Chromium–Aluminum Alloys. *Oxid. Met.* **2000**, *54*, 385–400. [CrossRef]
23. Sawada, H. An electron density residual study of α-ferric oxide. *Mater. Res. Bull.* **1996**, *31*, 141–146. [CrossRef]
24. Sasaki, S. Radial Distribution of Electron Density in Magnetite, Fe_3O_4. *Acta Cryst.* **1997**, *53*, 762–766. [CrossRef]
25. Geller, S. Structure of α-Mn_2O_3, $(Mn_{0.983}Fe_{0.017})2O_3$ and $(Mn_{0.37}Fe_{0.63})_2O_3$ and relation to magnetic ordering. *Acta Cryst.* **1971**, *27*, 821–828. [CrossRef]
26. Hugh-Jones, D.A.; Woodland, A.B.; Angel, R.J. The structure of high-pressure C_2/c ferrosilite and crystal chemistry of high-pressure C2/c pyroxenes. *Am. Min.* **1994**, *79*, 1032–1041. Available online: https://pubs.geoscienceworld.org/msa/ammin/article-abstract/79/11-12/1032/105232/The-structure-of-high-pressure-C2-c-ferrosilite (accessed on 10 September 2024)

27. Sitepu, H. Texture and structural refinement using neutron diffraction data from molybdite (MoO_3) and calcite ($CaCO_3$) powders and a Ni-rich $Ni_{50.7}Ti_{49.30}$ alloy. *Powder Diffr.* **2009**, *24*, 315–326. [CrossRef]
28. Lenaz, D.; Skogby, H.; Princivalle, F.; Falenius, U. Structural changes and valence states in the $MgCr_2O_4$–$FeCr_2O_4$ solid solution series. *Phys. Chem. Miner.* **2004**, *31*, 633–642. [CrossRef]
29. Smyth, J.R. High temperature crystal chemistry of fayalite. *Am. Min.* **1975**, *60*, 1092–1097.
30. Song, L.W.; Song, Y.W.; Shan, Y.; Zhu, G.Y.; Han, H. Product/metal ratio (PMR): A novel criterion for the evaluation of electrolytes on micro-arc oxidation (MAO) of Mg and its alloys. *Sci. China Technol. Sci.* **2011**, *54*, 2795–2801. [CrossRef]
31. Chou, K.C.; Luo, Q.; Li, Q.; Zhang, J.Y. Influence of the density of oxide on oxidation kinetics. *Intermetallics* **2014**, *47*, 17–22. [CrossRef]
32. Moon, C.O.; Lee, S.B. Analysis on failures of protective-oxide layers and cyclic oxidation. *Oxid. Met.* **1993**, *39*, 1–13. [CrossRef]
33. Zhang, C.; Zhang, Y.; Hu, J.; Wang, Z.; Xue, J.; Yu, H.; Zhang, C.; Wang, X.; Cai, Q.; Wang, C.; et al. Effect of Mo on the high-temperature oxidation behavior of Cr-Ni-Mo hot-work die steels. *Corros. Sci.* **2023**, *224*, 1–13. [CrossRef]
34. Xu, C.; Gao, W. Pilling-Bedworth ratio for oxidation of alloys. *Mater. Res. Innov.* **2000**, *3*, 231–235. [CrossRef]
35. Chaur, J.W.; Shih, M.C. The high-temperature oxidation behavior of hot-dipping Al–Si coating on low carbon steel. *Surf. Coat. Technol.* **2006**, *200*, 6601–6605. [CrossRef]
36. Matlakhov, A.N. *Corrosão e Proteção dos Materiais*; (Organização de Matlakhova L. A.); Paco Editorial: Jundiaí, São Paulo, Brazil, 2021.
37. Robertson, J.; Manning, M.I. Limits to adherence of oxide scales. *Mater. Sci. Technol. Ser.* **2013**, *6*, 81–92. [CrossRef]
38. Xu, L.N.; Guo, S.Q.; Chang, W.; Chen, T.H.; Hu, L.H.; Lu, M.X. Corrosion of Cr bearing low alloy pipeline steel in CO_2 environment at static and flowing conditions. *Appl. Surf. Sci.* **2013**, *270*, 395–407. [CrossRef]
39. Zhang, Y.; Zhang, C.; Li, F.; Wang, Z.; Wang, X.; Wang, C.; Zhang, C.; Huang, J.; Mao, F.; Chen, C.; et al. High-temperature oxidation behavior of Cr-Ni-Mo hot-work die steels. *Materials* **2022**, *15*, 5145. [CrossRef]
40. Hao, M.; Sun, B.; Wang, H. High-Temperature Oxidation Behavior of Fe–1Cr–0.2Si Steel. *Materials* **2020**, *13*, 509. [CrossRef]

Disclaimer/Publisher's Note: The statements, opinions and data contained in all publications are solely those of the individual author(s) and contributor(s) and not of MDPI and/or the editor(s). MDPI and/or the editor(s) disclaim responsibility for any injury to people or property resulting from any ideas, methods, instructions or products referred to in the content.